JOURNAL OF GEOPHYSICAL RESEARCH, VOL. 114, D22301, doi:10.1029/2009JD012287, 2009

Inverse modeling of global and regional CH_4 emissions using SCIAMACHY satellite retrievals

Peter Bergamaschi,[1] Christian Frankenberg,[2] Jan Fokke Meirink,[3] Maarten Krol,[2,4,5] M. Gabriella Villani,[1] Sander Houweling,[2,5] Frank Dentener,[1] Edward J. Dlugokencky,[6] John B. Miller,[6,7] Luciana V. Gatti,[8] Andreas Engel,[9] and Ingeborg Levin[10]

Received 20 April 2009; revised 23 June 2009; accepted 18 August 2009; published 17 November 2009.

[1] Methane retrievals from the Scanning Imaging Absorption Spectrometer for Atmospheric Chartography (SCIAMACHY) instrument onboard ENVISAT provide important information on atmospheric CH_4 sources, particularly in tropical regions which are poorly monitored by in situ surface observations. Recently, Frankenberg et al. (2008a, 2008b) reported a major revision of SCIAMACHY retrievals due to an update of spectroscopic parameters of water vapor and CH_4. Here, we analyze the impact of this revision on global and regional CH_4 emissions estimates in 2004, using the TM5-4DVAR inverse modeling system. Inversions based on the revised SCIAMACHY retrievals yield ~20% lower tropical emissions compared to the previous retrievals. The new retrievals improve significantly the consistency between observed and assimilated column average mixing ratios and the agreement with independent validation data. Furthermore, the considerable latitudinal and seasonal bias correction of the previous SCIAMACHY retrievals, derived in the TM5-4DVAR system by simultaneously assimilating high-accuracy surface measurements, is reduced by a factor of ~3. The inversions result in significant changes in the spatial patterns of emissions and their seasonality compared to the bottom-up inventories. Sensitivity tests were done to analyze the robustness of retrieved emissions, revealing some dependence on the applied a priori emission inventories and OH fields. Furthermore, we performed a detailed validation of simulated CH_4 mixing ratios using NOAA ship and aircraft profile samples, as well as stratospheric balloon samples, showing overall good agreement. We use the new SCIAMACHY retrievals for a regional analysis of CH_4 emissions from South America, Africa, and Asia, exploiting the zooming capability of the TM5 model. This allows a more detailed analysis of spatial emission patterns and better comparison with aircraft profiles and independent regional emission estimates available for South America. Large CH_4 emissions are attributed to various wetland regions in tropical South America and Africa, seasonally varying and opposite in phase with CH_4 emissions from biomass burning. India, China and South East Asia are characterized by pronounced emissions from rice paddies peaking in the third quarter of the year, in addition to further anthropogenic emissions throughout the year.

Citation: Bergamaschi, P., et al. (2009), Inverse modeling of global and regional CH_4 emissions using SCIAMACHY satellite retrievals, *J. Geophys. Res.*, *114*, D22301, doi:10.1029/2009JD012287.

1. Introduction

[2] Atmospheric CH_4 is the most important anthropogenic greenhouse gas (GHG) after CO_2, with a present direct radiative forcing of +0.48 ± 0.05 Wm^{-2} [*Forster et al.*, 2007]. This direct radiative forcing is further enhanced by four indirect radiative effects of CH_4 emissions: (1) the

[1]Institute for Environment and Sustainability, European Commission Joint Research Centre, Ispra, Italy.
[2]Netherlands Institute for Space Research, SRON, Utrecht, Netherlands.
[3]Royal Netherlands Meteorological Institute, De Bilt, Netherlands.
[4]Wageningen University and Research Centre, Wageningen, Netherlands.
[5]Institute for Marine and Atmospheric Research Utrecht, Utrecht, Netherlands.
[6]Global Monitoring Division, Earth System Research Laboratory, NOAA, Boulder, Colorado, USA.
[7]Cooperative Institute for Research in Environmental Sciences, University of Colorado at Boulder, Boulder, Colorado, USA.
[8]Instituto de Pesquisas Energeticas Nucleares, Pinheiros, Brazil.
[9]Institute for Atmosphere and Environment, J.W. Goethe University, Frankfurt am Main, Germany.
[10]Institut für Umweltphysik, University of Heidelberg, Heidelberg, Germany.

0148-0227/09/2009JD012287$09.00

increase of CH_4 lifetime due to feedbacks to the global OH concentration, (2) the effect on tropospheric ozone, (3) the increase in stratospheric water vapor, and (4) the generation of CO_2 as final product of the CH_4 oxidation chain, leading to a total emission-based radiative forcing of CH_4 of 0.86 Wm^{-2} [*Forster et al.*, 2007; *Shindell et al.*, 2005]. Based on the direct effect and the first 3 indirect effects, the estimated global warming potential of CH_4 (relative to CO_2) over a 100 year time horizon is 25 [*Forster et al.*, 2007].

[3] Compared to pre-industrial levels of 715 ± 4 ppb during 1700–1800 [*Etheridge et al.*, 1998] atmospheric CH_4 has increased by a factor of about 2.5. Ice core measurements reveal that present-day CH_4 mixing ratios are unprecedented during at least the last 800000 years [*Loulergue et al.*, 2008; *Spahni et al.*, 2005], with maximum values of up to 800 ppb measured for previous interglacial periods. Direct atmospheric observations since the late 1970s show a rapid increase of atmospheric CH_4 mixing ratios until 2000, and relatively stable CH_4 mixing ratios during the period 2000–2006 [*Blake and Rowland*, 1988; *Dlugokencky et al.*, 1994, 2003; *Forster et al.*, 2007]. Recent measurements, however, indicate that atmospheric CH_4 increased again significantly in 2007 [*Rigby et al.*, 2008]. At present it is unclear whether this increase is just a temporary anomaly (as observed e.g., in 2003) or the start of a new period of increasing CH_4 mixing ratios.

[4] The major sink of atmospheric CH_4 is reaction with OH radicals constituting about 90% of total sink. The global annual total of the OH sink is believed to be relatively well known (∼±10%), mainly based on atmospheric measurements and emission data of methyl chloroform [*Bousquet et al.*, 2005; *Intergovernmental Panel on Climate Change* (*IPCC*), 2007; *Krol and Lelieveld*, 2003]. Further smaller atmospheric CH_4 sinks are oxidation in aerobic soils, destruction by Cl radicals in the marine boundary layer, and reaction with Cl and $O(^1D)$ radicals in the stratosphere. Since the global CH_4 burden is well known from atmospheric measurements, total global emissions can be estimated rather accurately to be ∼500–600 Tg CH_4/yr [*Forster et al.*, 2007].

[5] Very large uncertainties, however, exist about the relative contributions from different source categories and the spatial and temporal distributions of their emissions. These uncertainties are mainly due to the typically very large variability of emissions of many CH_4 source categories, leading to large uncertainties of bottom-up estimates based on activity data and emission factors, or based on biogeochemical models.

[6] Complementary to bottom-up estimates, atmospheric measurements combined with inverse atmospheric models can provide independent top-down estimates of emissions and their spatiotemporal patterns, tracing back the observed atmospheric signals to the origin of emissions. Inverse modeling based top-down estimates have been widely used for the most important anthropogenic GHGs, including CO_2 [*Gurney et al.*, 2002; *Rödenbeck et al.*, 2003; *Stephens et al.*, 2007], CH_4 [*Bergamaschi et al.*, 2007; *Bousquet et al.*, 2006; *Chen and Prinn*, 2006; *Hein et al.*, 1997; *Houweling et al.*, 1999; *Mikaloff Fletcher et al.*, 2004a, 2004b], N_2O [*Hirsch et al.*, 2006; *Huang et al.*, 2008; *Prinn et al.*, 1990], and several CFCs and HFCs [*Manning et al.*, 2003; *Stemmler et al.*, 2007]. Initially most inverse modeling studies focused on emission estimates on continental scales, using global surface measurements (mainly from marine and continental background stations). Various recent studies demonstrated that regional top-down estimates can also be provided (e.g., on the spatial scales of individual countries) using high-resolution models and better coverage of measurements [*Bergamaschi et al.*, 2005; *Manning et al.*, 2003]. Such regional top-down estimates are also very important in the context of verification of international agreements on emission reductions, such as the United Nations Framework Convention on Climate Change (UNFCCC) and the Kyoto protocol [*Bergamaschi*, 2007; *IPCC*, 2000].

[7] Globally, however, the network of surface measurements for the major GHGs is still very sparse with large continental areas remaining poorly monitored. This is especially true for tropical regions, where strong convection transports emissions aloft resulting in generally very low signals at remote marine observation sites. Therefore, satellite measurements with quasi-global coverage provide a very attractive complement to the surface network. The major challenge for long-lived GHG measurements from space is the demanding requirements on precision and accuracy to detect the small spatial and temporal gradients in the atmosphere. Such spaceborne measurements have become available for CH_4 from the Scanning Imaging Absorption Spectrometer for Atmospheric Chartography (SCIAMACHY) instrument onboard ESA's environmental satellite ENVISAT, with an estimated relative accuracy on the order of 1–2% [*Frankenberg et al.*, 2005, 2006; *Schneising et al.*, 2009]. However, the accurate quantification of potential systematic errors for satellite retrievals remains very difficult because of the complexity of the retrieval algorithms and the limited availability of independent validation measurements. First inverse modeling studies using these CH_4 retrievals were presented by *Bergamaschi et al.* [2007] and *Meirink et al.* [2008a], suggesting significantly larger tropical CH_4 emissions than estimated by current bottom-up inventories and derived from inversions based on global surface monitoring sites only.

[8] Recently, *Frankenberg et al.* [2008a] reported a major revision of their CH_4 retrievals, resulting in significantly lower column-averaged CH_4 mixing ratios especially in the tropics. This revision has been mainly the consequence of the identification of systematic errors in the spectroscopic parameters of CH_4 [*Frankenberg et al.*, 2008b] and H_2O vapor [*Frankenberg et al.*, 2008a]. In particular the latter led to interference between H_2O and CH_4 in the previous retrievals, an effect which was most pronounced in tropical regions due to large H_2O vapor abundances. First assimilations of the revised retrievals using our TM5 four-dimensional variational (TM5-4DVAR) inverse modeling system [*Meirink et al.*, 2008b] indicated a significant reduction of derived tropical emissions [*Frankenberg et al.*, 2008a]. In this paper we now present a detailed evaluation of the new retrievals and their impact on derived CH_4 emissions. For this purpose we apply a further developed version of the TM5-4DVAR system, which allows the suppression of negative a posteriori emissions, an artifact sometimes encountered when using Gaussian a priori error distributions and strongly constraining observational data. Furthermore the updated TM5-4DVAR system includes a

Table 1. Surface Air Sampling Sites From the NOAA Network Used in the Inversions

Identification	Station Name	Latitude (deg)	Longitude (deg)	Altitude (masl)
ALT	Alert, Nunavut, Canada	82.45	−62.52	210
ZEP	Ny-Alesund, Svalbard (Spitsbergen), Norway and Sweden	78.90	11.88	475
SUM	Summit, Greenland	72.58	−38.48	3238
BRW	Barrow, Alaska, USA	71.32	−156.60	11
STM	Ocean station M, Norway	66.00	2.00	5
ICE	Heimay, Vestmannaeyjar, Iceland	63.34	−20.29	127
CBA	Cold Bay, Alaska, USA	55.20	−162.72	25
SHM	Shemya Island, Alaska, USA	52.72	174.10	40
UUM	Ulaan Uul, Mongolia	44.45	111.10	914
KZM	Plateau Assy, Kazakhstan	43.25	77.88	2519
NWR	Niwot Ridge, Colorado, USA	40.05	−105.58	3526
AZR	Terceira Island, Azores, Portugal	38.77	−27.38	40
WLG	Mt. Waliguan, Peoples Republic of China	36.29	100.90	3810
BMW	Tudor Hill, Bermuda, UK	32.27	−64.88	30
IZO	Tenerife, Canary Islands, Spain	28.30	−16.48	2360
MID	Sand Island, Midway, USA	28.22	−177.37	8
ASK	Assekrem, Algeria	23.18	5.42	2728
MLO	Mauna Loa, Hawaii, USA	19.53	−155.58	3397
KUM	Cape Kumukahi, Hawaii, USA	19.52	−154.82	3
GMI	Mariana Islands, Guam	13.43	144.78	6
RPB	Ragged Point, Barbados	13.17	−59.43	45
CHR	Christmas Island, Republic of Kiribati	1.70	−157.17	3
SEY	Mahe Island, Seychelles	−4.67	55.17	7
ASC	Ascension Island, UK	−7.92	−14.42	54
SMO	Tutuila, American Samoa, USA	−14.23	−170.57	42
EIC	Easter Island, Chile	−27.15	−109.45	50
CRZ	Crozet Island, France	−46.45	51.85	120
TDF	Tierra Del Fuego, La Redonda Isla, Argentina	−54.87	−68.48	20
PSA	Palmer Station, Antarctica, USA	−64.92	−64.00	10
SYO	Syowa Station, Antarctica, Japan	−69.00	39.58	14
HBA	Halley Station, Antarctica, UK	−75.58	−26.50	33
SPO	South Pole, Antarctica, USA	−89.98	−24.80	2810

better representation of the SCIAMACHY measurements and their uncertainties.

[9] The specific objectives of this paper are: (1) to analyze the impact of the revision of the SCIAMACHY retrievals on emissions attributed to large global regions, especially the tropics; (2) to investigate the robustness of derived emissions through sensitivity experiments, in which key assumptions of the inversions are varied; (3) to validate 3D CH_4 model fields with independent observational data sets; and (4) to analyze the impact of the revised SCIAMACHY retrievals on regional inversions for South America, Africa, and Asia, using the zooming capability of the TM5 model.

2. Measurements

2.1. SCIAMACHY Measurements

[10] In this study, we use the recently revised CH_4 retrievals from SCIAMACHY (Iterative Maximum A Posteriori Version 5.0 (IMAP V5.0)), as described by *Frankenberg et al.* [2008a]. The most important difference from the previous published CH_4 retrievals (version V1.1, described by *Frankenberg et al.* [2006] and applied by *Bergamaschi et al.* [2007] and *Meirink et al.* [2008a]) is the use of updated spectroscopic parameters for CH_4 and H_2O, largely eliminating the dependence of retrieved CH_4 values on atmospheric H_2O abundance. Further improvements in the new CH_4 retrievals consist of the use of European Centre for Medium-Range Weather Forecasts (ECMWF) pressure and temperature profiles, and CH_4 profiles from a TM5-4DVAR inversion (based on surface measurements only) as a priori information in the retrieval algorithm. These a priori CH_4 profiles are taken from the TM5-4DVAR fields at longitude 180° W (basically over the background ocean), to avoid any impact of the longitudinal variability of the TM5-4DVAR fields on the SCIAMACHY retrievals.

[11] As in the previous product, total columns of CH_4 (denoted VCH_4) and CO_2, VCO_2, are derived from neighboring spectral regions in SCIAMACHY channel 6 (fitting window: CH_4: 1631–1670 nm; CO_2: 1563–1585 nm), but the column-averaged CH_4 mixing ratio, XCH_4, is now obtained by using the CO_2 model fields from NOAA's CarbonTracker product [*Peters et al.*, 2007], which are assimilated CO_2 fields based on NOAA's global network of CO_2 measurements and an Ensemble Kalman Filter system based on the TM5 model [*Peters et al.*, 2005]:

$$XCH_4 = \frac{VCH_4}{VCO_2} \cdot XCO_{2\text{CarbonTracker}} \quad (1)$$

Since SCIAMACHY measurements over the ocean are restricted to conditions with either low lying clouds, sun glint or a very rough ocean surface, small systematic differences between the SCIAMACHY measurements over land and over the ocean cannot be ruled out. Small land-ocean biases in the SCIAMACHY retrievals are indeed suggested by our sensitivity experiment S7, in which both land and ocean pixels were used (section 4.1.3). Apart from

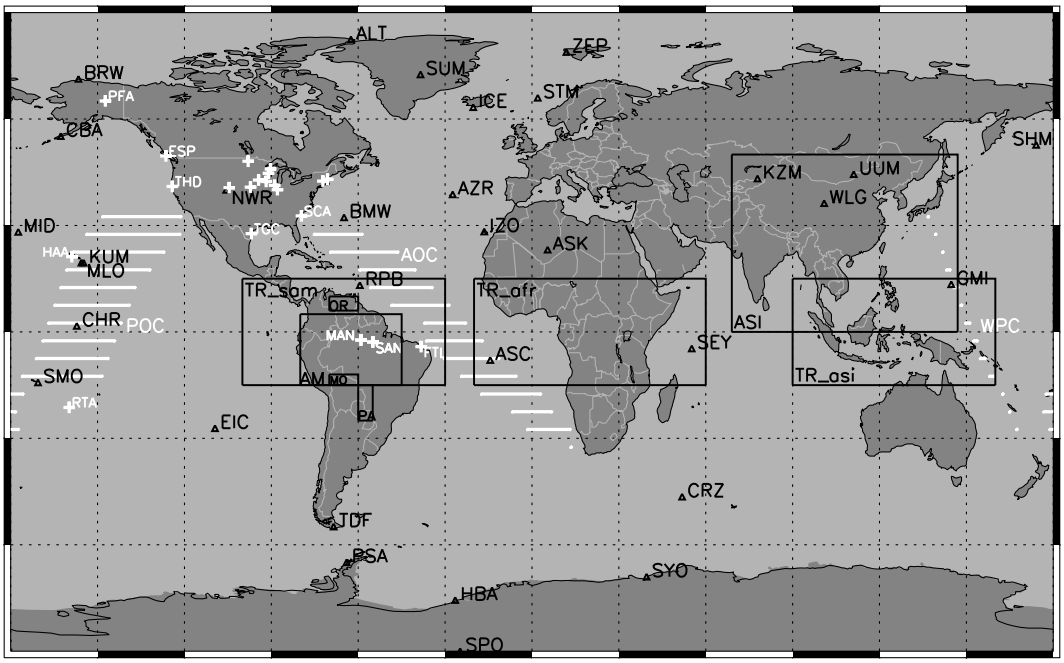

Figure 1. NOAA surface sites used in the inversions (black triangles with black identifiers). Furthermore, regions of ship cruises (POC, AOC, and WPC; white lines, indicating the longitudinal range within each 5° latitude range) and locations of aircraft profiles (white crosses) used for validation are shown. Rectangles (TR_sam, TR_afr, TR_asi, ASI) display various regions for which total emissions have been calculated (Table 7). The smaller rectangles over South America indicate various wetland regions (AM, Amazon; MO, Mojos; OR, Orinoco; PA, Pantanal; see Table 8).

this sensitivity test, we generally only use the SCIAMACHY pixels over land in this study.

2.2. Ground-Based Measurements

[12] Surface observations of CH_4 mixing ratios are from the NOAA Earth System Research Laboratory (ESRL) global cooperative air sampling network [*Dlugokencky et al.*, 1994, 2003]. Here we use the same set of 32 sites for the inversions as used by *Bergamaschi et al.* [2007] and *Meirink et al.* [2008a] (see Table 1). This set of sites includes only marine and continental background sites in the inversion, omitting sites which are difficult to simulate with the $6° \times 4°$ coarse grid version of the TM5 model, e.g., some coastal sites (e.g., Mace Head (MHD) and Cape Grim (CGO)) or sites which are significantly influenced by regional sources (e.g., Baltic Sea (BAL) and Black Sea (BSC)). Measurements are reported relative to the NOAA04 calibration scale [*Dlugokencky et al.*, 2005].

2.3. Further Measurements Used for Validation

[13] Various additional data sets have been used for validation of the simulated 3D CH_4 mixing ratio fields. These data sets include NOAA ESRL measurements of flask samples taken from regular ship cruises in the Atlantic Ocean (AOC), Pacific Ocean (POC), and West Pacific ocean (WPC) (see Figure 1), mainly serving to validate simulated surface mixing ratios over the remote ocean and downwind the continental sources. For validation of simulated vertical gradients in the troposphere, we use a large number of NOAA aircraft profiles, mainly over the mainland United States, but also including further sites in Canada, Alaska, and the Pacific Ocean (see Table 2 and Figure 1). Moreover, we use the NOAA/Instituto de Pesquisas Energeticas Nucleares (IPEN) aircraft profiles at 3 sites in South America, which are sensitive to emissions from the Amazon region [*Miller et al.*, 2007]. For validation of stratospheric CH_4 mixing ratios we use measurements taken from balloon soundings (compiled in Table 3) in the

Table 2. Aircraft Profiles Used for Validation

Identification	Station Name	Latitude (deg)	Longitude (deg)
PFA	Poker Flat, Alaska, USA	65.1	−147.3
ESP	Estevan Point, British Columbia, Canada	49.6	−126.4
DND	Dahlen, North Dakota, USA	48.1	−98.0
LEF	Park Falls, Wisconsin, USA	45.9	−90.3
FWI	Fairchild, Wisconsin, USA	44.7	−91.0
NHA	Worcester, Massachusetts, USA	43.0	−70.6
BGI	Bradgate, Iowa, USA	42.8	−94.4
HFM	Harvard Forest, Massachusetts, USA	42.5	−72.2
WBI	West Branch, Iowa, USA	42.4	−91.8
OIL	Oglesby, Illinois, USA	41.3	−88.9
THD	Trinidad Head, California, USA	41.0	−124.2
BNE	Beaver Crossing, Nebraska, USA	40.8	−97.2
CAR	Briggsdale, Colorado, USA	40.6	−104.6
HIL	Homer, Illinois, USA	40.1	−87.9
SCA	Charleston, South Carolina, USA	32.7	−79.6
TGC	Sinton, Texas, USA	27.7	−96.9
HAA	Molokai Island, Hawaii, USA	21.2	−158.9
MAN	Manaus, Brazil	−2.3	−59.0
SAN	Santarem, Brazil	−2.8	−55.0
FTL	Fortaleza, Brazil	−4.2	−38.3
RTA	Rarotonga, Cook Islands	−21.3	−159.8

Table 3. Stratospheric Balloon Profiles Used for Validation

Identification	Location	Latitude (deg)	Longitude (deg)	Date
B34	Kiruna, Sweden	67.3–68.3°N	21.2–27.9°E	06.02.1999
B35	Aire sur l'Adour, France	43.8–44.0°N	0.1–0.4°E	03.05.1999
B36	Kiruna, Sweden	67.6–68.8°N	21.8–28.1°E	27.01.2000
B37	Kiruna, Sweden	68.0–68.0°N	24.0–27.7°E	01.03.2000
B38	Aire sur l'Adour, France	44.0–44.2°N	0.7–1.3°E	09.10.2001
B39	Aire sur l'Adour, France	43.4–43.5°N	0.2°W–1.2°E	24.09.2002
B40	Kiruna, Sweden	66.8–67.9°N	22.1–26.8°E	06.03.2003
B41	Kiruna, Sweden	67.8–67.9°N	19.7–20.7°E	09.06.2003
B42	Teresina, Brazil	5.3–5.1°S	43.4–45.3°W	08.06.2005
B43	Teresina, Brazil	5.3–5.1°S	43.4–45.3°W	25.06.2005

period 1999–2005 [*Engel et al.*, 2006, 2009], analyzed at the University of Heidelberg, Germany.

3. Modeling

3.1. TM5-4DVAR Inverse Modeling System

[14] We employ a further developed 4DVAR inverse modeling system, based on the 4DVAR system described in detail by *Meirink et al.* [2008b]. In the following we summarize the major components of the previous system, and describe the new developments.

[15] 4DVAR is a variational optimization technique, which was originally developed in Numerical Weather Prediction [*Courtier et al.*, 1994]. It allows optimization of a very large number of parameters using at the same time very large sets of observational data, such as satellite data. In recent years the 4DVAR technique has been adapted for inverse modeling [*Chevallier et al.*, 2005; *Meirink et al.*, 2008b; *Stavrakou and Müller*, 2006]. The optimal set of model parameters (state vector $\boldsymbol{x}$) is obtained by iteratively minimizing the cost function:

$$J(\boldsymbol{x}) = \frac{1}{2}(\boldsymbol{x}-\boldsymbol{x}_B)^{\mathrm{T}}\mathbf{B}^{-1}(\boldsymbol{x}-\boldsymbol{x}_B) + \frac{1}{2}\sum_{i=1}^{n}(H_i(\boldsymbol{x})-\boldsymbol{y_i})^{\mathrm{T}}\mathbf{R_i^{-1}}(H_i(\boldsymbol{x})-\boldsymbol{y_i}) \quad (2)$$

where $\boldsymbol{x}_B$ is the a priori estimate of $\boldsymbol{x}$, and $\mathbf{B}$ the parameter error covariance matrix (containing the uncertainties of the parameters and their correlations in space and time). $\boldsymbol{y}$ denotes the set of observational data, $\mathbf{R}$ their corresponding error covariance matrix, and $H(\boldsymbol{x})$ the model simulations corresponding to the observations. The assimilation is discretized into small assimilation time slots, denoted by index i in equation (2). For the individual time slots, observations and model values are averaged over the length of the time slot.

[16] In our application the whole integration time is 14 months, and the length of the assimilation time slots is set to 3 h. The state vector $\boldsymbol{x}$ is made up by three sets of parameters: (1) initial 3D atmospheric mixing ratios, (2) monthly emissions per model grid cell and emission category, and (3) further parameters for bias corrections of satellite data.

[17] The minimization algorithm requires the evaluation of the gradient of the cost function with respect to the state vector:

$$\nabla J(\boldsymbol{x}) = \mathbf{B}^{-1}(\boldsymbol{x}-\boldsymbol{x}_B) + \sum_{i=1}^{n}\mathbf{H_i^T}\mathbf{R_i^{-1}}(H_i(\boldsymbol{x})-\boldsymbol{y_i}) \quad (3)$$

where $\mathbf{H^T}$ is the adjoint of the model operator. In the previous system [*Meirink et al.*, 2008b], the model operator was strictly linear, and hence $\mathbf{H^T}$ the adjoint of the forward model operator. With the further development of our 4DVAR system (as described below), the forward model is no longer linear, and therefore $\mathbf{H^T}$ represents the adjoint of the tangent linear forward model. In the linear case the cost function is minimized using the ECMWF conjugate gradient algorithm [*Fisher and Courtier*, 1995].

[18] Our 4DVAR system applies the atmospheric transport model TM5 [*Krol et al.*, 2005], which is an offline transport model, driven by meteorological fields (6 h forecasts) from the European Centre for Medium Range Weather Forecasts (ECMWF) operational Integrated Forecast System (IFS) model. TM5 has a two-way nested zooming capability, which allows it to perform higher horizontal resolution simulations in specified 3° × 2° and 1° × 1° nested grids, embedded into the global domain, simulated at 6° × 4° resolution. Because of the high computational costs of the 4DVAR simulations we use the 6° × 4° resolution only for our global analysis and the various sensitivity experiments. For the regional analysis the 1° × 1° zooming is applied over South America, Africa, and Asia, as further detailed in section 3.3 and Table 5.

[19] We employ the standard TM5 version (TM5 cycle 1), with 25 vertical layers, defined as a subset of the 60 layers used operationally in the ECMWF IFS model until 2006. The generation of the adjoint of the TM5 model is described in detail by *Krol et al.* [2008] and *Meirink et al.* [2008b].

[20] For the present study, the following further developments of the TM5-4DVAR system have been applied:

3.1.1. Implementation of Nonlinear 4DVAR System to Avoid Negative a Posteriori Emissions

[21] The previous system assumed a Gaussian probability density function (PDF) for the a priori emissions. In case of uncertainties that are of the same order of magnitude as the emissions themselves (which is typically assumed for CH_4 emissions), this implies a nonnegligible probability that emissions become negative. In fact, negative a posteriori emissions were sometimes obtained with the previous TM5-4DVAR system in some regions, in particular when strongly constraining observational data sets were applied, expressing a compensation for observational and model errors. In some cases, this artifact in the derived emissions also created significant artifacts in the simulated CH_4 mixing ratios, namely considerable CH_4 depletions close to regions of negative emissions.

[22] To enforce that a posteriori emissions remain positive, we apply a 'semiexponential' description of the PDF:

$$\begin{aligned} e &= e_{apri0} * \exp(x) \qquad for\ x < 0 \\ e &= e_{apri0} * (1 + x) \qquad for\ x > 0 \end{aligned} \tag{4}$$

where the a priori emissions e_{apri0} are used as a constant, and the emission parameter x is optimized instead. x is set a priori to zero, and assumed to have a Gaussian PDF. We chose this 'semiexponential' approach in contrast to a regular exponential function as applied e.g., by *Müller and Stavrakou* [2005], in order to avoid an increase in the PDF for emissions higher than the a priori emissions. Furthermore, test inversions showed somewhat better convergence of the minimization algorithm for the 'semiexponential' function compared to a regular exponential function.

[23] This 'semiexponential' approach introduces a nonlinearity of the forward model operator. While the tangent linear model corresponding to equation (4) and its adjoint can be readily obtained, the nonlinearity of the whole model operator H made a major update of the optimization procedure necessary (since the conjugate gradient algorithm can handle only linear systems). Therefore, a system with an outer loop for evaluation of the nonlinear model and an inner loop for incremental optimization of the linearized model has been implemented, similar to the ECMWF operational 4DVAR system [*Tremolet*, 2007] (but with same model resolution in the outer and inner loop). For the incremental optimization in the inner loop the ECMWF conjugate gradient algorithm [*Fisher and Courtier*, 1995] is used. After each inner loop cycle, the state vector for the outer loop evaluation of the nonlinear model, $\boldsymbol{x}_{NL(i+1)}$, is updated by the increment derived in the inner loop, $\delta\boldsymbol{x}_{LI}$:

$$\boldsymbol{x}_{NL(i+1)} = \boldsymbol{x}_{NL(i)} + \delta\boldsymbol{x}_{LI}$$

A disadvantage of the new system is that currently no a posteriori uncertainty estimates can be provided, since the number of iterations applied in the inner loop (as detailed in section 3.2) is not sufficient to reach satisfactory convergence of the approximation of the a posteriori uncertainties based on the leading Eigenvectors [*Meirink et al.*, 2008b].

3.1.2. Improved Representation of Measurements and Their Errors

[24] As in our previous studies [*Bergamaschi et al.*, 2007; *Meirink et al.*, 2008a] we generally include high-accuracy surface measurements in the inversions of the SCIAMACHY data to derive and correct potential biases of the SCIAMACHY retrievals. This bias correction is modeled as a second order polynomial as function of latitude and month. To minimize the impact of potential systematic errors in simulated stratospheric CH_4 mixing ratios at higher latitudes, we limit the use of the SCIAMACHY data to the latitude region between 50°S and 50°N, where comparison of modeled CH_4 in the stratosphere with observations indicates generally good agreement (see section 4.2.3).

[25] Individual SCIAMACHY pixels have an extension of 30 km (along track) times 60 km (across track), and the column-averaged CH_4 mixing ratios, XCH_4, retrieved for these pixels are averaged on a regular 1° × 1° (longitude × latitude) grid. Modeled CH_4 fields are interpolated from the model resolution to the same 1° × 1° grid, and vertically integrated using the averaging kernels specified for the SCIAMACHY retrievals to obtain the column-averaged mixing ratio, $XCH_{4(TM5)}$ [see also *Bergamaschi et al.*, 2007; *Frankenberg et al.*, 2006].

[26] Systematic errors may arise from the difference in horizontal resolution between observations and model, particularly in the case of complex topography. We therefore introduce a surface elevation filter to ensure that the atmospheric columns seen by SCIAMACHY are well represented by the model columns. This filter requests that the difference between surface elevation of the SCIAMACHY pixel, $h_{surface(SCIAMACHY)}$, and that of the model grid cell, $h_{surface(TM5)}$, is within a specified limit

$$\left|h_{surface\ (SCIAMACHY)} - h_{surface\ (TM5)}\right| < dh_{\mathrm{MAX}}$$

We set dh_{MAX} to 250 m as default value, leading typically to the rejection of 17% of the SCIAMACHY data over land.

[27] While in the previous studies the uncertainty of the SCIAMACHY retrievals was assumed to be constant, we take now explicitly the contributions from the estimated random and systematic errors into account:

$$\Delta XCH_{4(tot)} = \left[\Delta XCH^2_{4(retrieval)} + \Delta XCH^2_{4(STD)} + \Delta XCH^2_{4(systematic\ error)}\right]^{1/2}$$

where $\Delta XCH_{4(retrieval)}$ is the statistical fit error (mainly related to the signal-to-noise ratio of the recorded spectra [*Frankenberg et al.*, 2006]) of the individual SCIAMACHY pixels, averaged over the 3h assimilation time slot and 1° × 1° grid, and $\Delta XCH_{4(STD)}$ is the standard deviation of the pixels over this averaging period and domain. $\Delta XCH_{4(systematic\ error)}$ is meant to represent systematic errors not covered by our bias correction, such as e.g., remaining systematic errors due to aerosols or surface albedo [*Frankenberg et al.*, 2006], and is set to an assumed constant value of 1%.

[28] Furthermore, we apply a new scheme to estimate the model representativeness error for surface stations. This new scheme includes estimates of the impact of the subgrid-scale variability of emissions on simulated mixing ratios for stations in the boundary layer. In the present study, however, the effect of this new scheme on retrieved emissions is relatively small, mainly because we use here only remote sites, for which emission of the local model grid cells play a minor role only. The details of the new scheme will be discussed in more detail elsewhere.

3.2. Inversion Setup

[29] The bottom-up inventories used as a priori estimates of the emissions are compiled in Table 4. In contrast to our previous study [*Meirink et al.*, 2008a] we do not optimize all source categories independently, but group the emissions into 3 classes: (1) wetland and rice, (2) biomass burning, and (3) all remaining sources. While emissions from 'wetlands and rice' and 'biomass burning' are characterized by pronounced seasonal variations (which are typically opposite in phase), all other sources can be assumed to be

Table 4. A Priori Bottom-Up Inventories and a Priori Annual Total Emissions

Source Category	Reference	Emission (Tg CH_4/yr)
Wetlands and rice		
Wetlands	'JK' inventory [*Bergamaschi et al.*, 2007][a]	174.9
Rice	GISS [*Matthews et al.*, 1991]	59.7
Biomass burning		
Biomass burning	GFEDv2 [*van der Werf et al.*, 2004]	20.1
Remaining sources		
Coal mining	EDGARV3.2FT [*Olivier and Berdowski*, 2001][b]	33.2
Oil production, transmission and handling	EDGARV3.2FT [*Olivier and Berdowski*, 2001][b]	10.4
Gas production and transmission	EDGARV3.2FT [*Olivier and Berdowski*, 2001][b]	48.7
Fossil fuel use	EDGARV3.2FT [*Olivier and Berdowski*, 2001][b]	3.4
Industrial processes	EDGARV3.2FT [*Olivier and Berdowski*, 2001][b]	0.9
Biofuel	EDGARV3.2FT [*Olivier and Berdowski*, 2001][b]	14.9
Enteric fermentation	EDGARV3.2FT [*Olivier and Berdowski*, 2001][b]	80.4
Animal waste management	EDGARV3.2FT [*Olivier and Berdowski*, 2001][b]	8.5
Waste handling	EDGARV3.2FT [*Olivier and Berdowski*, 2001][b]	58.1
Wild animals	[*Houweling et al.*, 1999]	5.0
Termites	[*Sanderson*, 1996]	19.4
Ocean	[*Houweling et al.*, 1999; *Lambert and Schmidt*, 1993]	17.0
Soil sink	[*Ridgwell et al.*, 1999]	−38.0
Total		516.5

[a]Three month running mean applied.
[b]Reference year 2000.

approximately constant throughout the year. Hence the seasonal variation of the atmospheric signal contains some information about the partitioning among these three classes, while any further differentiation among the individual source categories requires a clear spatial separation, and good a priori knowledge of the location of the sources.

[30] We optimize monthly mean emissions and set the temporal correlations for 'wetlands and rice' and 'biomass burning' to zero, hence allowing maximum flexibility to optimize the seasonal variation proposed by the a priori inventories. The temporal correlation for 'remaining emissions' is set to 9.5 months to suppress unexpected large seasonal variations of this emission class. The spatial correlation lengths are set to 500 km for the global coarse resolution ($6^\circ \times 4^\circ$) inversions and to 300 km for the inversions with $1^\circ \times 1^\circ$ zooming (see also section 3.3 and Table 5). The uncertainties of the emission parameter x (equation (4)) are set to 100% per grid cell for 'wetlands and rice' and 'biomass burning', and to 50% for 'remaining emissions'.

[31] Chemical destruction of CH_4 by OH radicals in the troposphere is simulated using precalculated OH fields based on Carbon Bond Mechanism 4 (CBM-4) chemistry and optimized with methyl chloroform [*Bergamaschi et al.*, 2005; *Houweling et al.*, 1998], resulting in a mean lifetime of tropospheric CH_4 versus tropospheric OH of 9.4 yrs. Chemical destruction of CH_4 by OH, Cl, and $O(^1D)$ in the stratosphere is based on the 2-D photochemical Max-Planck-Institute (MPI) model [*Brühl and Crutzen*, 1993]. The prescribed concentrations of the radicals are not optimized in the inversion.

[32] Inversions are run over 14 months starting 01 December 2003. The initial CH_4 mixing ratio fields are from a previous inversion (over the year 2003). Although this initial field is further optimized in the inversion, the resulting inversion increments are generally very small.

[33] The inversions are performed in 3 cycles.

[34] 1. A first cycle in which initial mixing ratio, emissions, and bias correction are optimized. This requires usually a relatively large number of inner loop iterations (typically 4 outer loop iterations and 60 inner loop iterations).

[35] 2. In a second cycle the bias correction calculated in the first cycle is fixed, and only initial mixing ratio and emissions are further optimized (using 8 outer loop iter-

Table 5. Reference Inversion and Sensitivity Inversions

Inversion	SCIAMACHY	Zoom	L_corr	Description
S1	IMAP V5.0		500 km	reference inversion
S2	IMAP V1.1		500 km	
S3			500 km	use of NOAA surface sites only
S4	IMAP V5.0		100 km	as S1, but spatial correlation length 100 km
S5	IMAP V5.0		500 km	as S1, but constant bias instead of 2nd order polynomial
S6	IMAP V5.0		500 km	as S1, but OH fields from *Spivakovsky et al.* [2000]
S7	IMAP V5.0		500 km	as S1, but include also SCIAMACHY data over ocean
S8	IMAP V5.0		300 km	as S1, but homogeneous emissions over land/over ocean resp.
S1Z	IMAP V5.0	sam1×1 afr1×1 asi1×1	300 km	as S1, but 1 × 1 zoom, spatial correlation length 300 km
S2Z	IMAP V1.1	sam1×1	300 km	
S3Z		sam1×1	300 km	use of NOAA surface stations only
S8Z	IMAP V5.0	sam1×1	50 km	as S1Z, but homogeneous emissions over land/over ocean resp.

ations and 10 inner loop iterations), generally further improving the convergence compared to the first cycle.

[36] 3. Observational data for which simulated mixing ratios differ by more than 3 sigma are rejected (typically ~0.25% of the data) and subsequently the second cycle is repeated. The rationale behind this data rejection is to avoid single outliers introducing significant biases into the inversion. In the present study, however, the impact of data rejection on derived emissions is generally very small.

3.3. Reference and Sensitivity Inversions

[37] The reference inversion (denoted S1) is based on the new SCIAMACHY retrievals IMAP V5.0. The sensitivity inversion S2 is using the previous product IMAP V1.1, while in S3 only the NOAA surface measurements are used and no satellite data (see Table 5). Note that the NOAA surface measurements are generally used in all inversions. In the sensitivity experiments S4–S8 again the IMAP V5.0 data set is applied, but various parameters have been varied: In sensitivity experiment S4 the spatial correlation length has been reduced from 500 km to 100 km, and in S5 we assess the sensitivity of the inversions to the assumptions on the bias correction, replacing the second order polynomial as function of latitude by a (monthly) constant bias. In S6 the sensitivity of results to the applied OH sink is investigated, using the OH fields from *Spivakovsky et al.* [2000] instead of those from TM5. In S7 we use also SCIAMACHY pixels over the ocean in the inversion to study the impact of a potential land-ocean bias of the SCIAMACHY retrievals. In inversion S8 the sensitivity of results to the applied a priori inventory is explored, replacing the standard bottom-up inventory (as compiled in Table 4) by the simple assumption of constant emissions over land, except Antarctica (with annual total emissions of 500 Tg CH_4/yr), and small constant emissions over the ocean (annual total 17 Tg CH_4/yr).

[38] In the S1Z inversions the $1^\circ \times 1^\circ$ zooming over South America, Africa, and Asia, respectively, has been used to investigate the regional spatial patterns in more detail and to allow better comparison with independent regional emission estimates. In these zoom inversions the spatial correlation length has been reduced to 300 km (but otherwise settings of the S1Z inversions are identical to the reference inversion S1). Likewise, sensitivity inversions S2Z, S3Z, and S8Z apply the $1^\circ \times 1^\circ$ zooming over South America and reduced correlation lengths, but use otherwise the settings of the corresponding coarse resolution inversions S2, S3, and S8. All zoom inversions have been split into 2 overlapping run periods (01 Dec 2003 to 01 Aug 2004, and 01 Jun 2004 to 01 Feb 2005) because of their very high CPU time demands.

4. Results and Discussion

4.1. Global Inversions

4.1.1. Reference Inversion S1

[39] Figure 2 shows column-averaged CH_4 mixing ratios, XCH_4, for year 2004 (3 month composite averages): IMAP V5.0 retrievals (Figure 2, left), and assimilated values (Figure 2, right). The small bias correction derived by TM5-4DVAR has been subtracted from the retrievals (see below). In general, the major regional patterns and their seasonal variation apparent in the retrievals are well captured in the assimilated XCH_4 fields, demonstrating the major progress of the 4DVAR system compared to the previously applied synthesis inversion [*Bergamaschi et al.*, 2007]. Some smaller-scale enhancements in the retrievals (e.g., over Venezuela and Columbia), however, are somewhat less pronounced in the assimilated fields, partly due to the coarse model resolution applied here ($6^\circ \times 4^\circ$).

[40] In Figure 3 we show the spatial and seasonal distribution of emissions and the partitioning among the 3 principal source categories which have been optimized (Figure 3, left: a priori; Figure 3, right: a posteriori). The a priori 'remaining emissions' vary very little with season (only the included soil sink is varying with season), and have their maximum between ~20°N and ~60°N. These principal patterns remain also in the a posteriori emissions. However, the 'remaining emissions' attributed to the Southern hemisphere are somewhat higher than in the a priori inventory. Emissions from 'wetlands and rice' and 'biomass burning' show a large seasonal variability. In particular, wetland emissions in tropical wet-dry climate regions largely follow the respective wet seasons, while wetland emissions in the continuously humid inner tropical zones persist during the whole year. This general seasonal behavior is clearly visible also in the a posteriori emissions, but a posteriori values of tropical emissions are generally higher compared to a priori values (see also Tables 6 and 7). Emissions from NH extratropical wetland regions and from rice paddies in India and South East Asia exhibit a very pronounced seasonality, however with significant differences between a priori and a posteriori distributions. The inversion leads to a significant reduction of NH extratropical wetland emissions in particular during the second quarter of the year, and an earlier end-of-season decline of rice emissions (with much lower values compared to the a priori inventories during the last quarter of the year), consistent with our previous results based on the IMAP V1.1 retrievals [*Bergamaschi et al.*, 2007]. Emissions from biomass burning represent only a small part of the annual total emissions, but constitute a significant source in the tropics during the respective NH and SH dry seasons, opposite in phase with the tropical wetland emissions. The inversion leads to a moderate enhancement of biomass burning emissions mainly in the SH dry season (July–September).

[41] In addition to changes in the seasonality, the inversion also leads to significant changes in the spatial emission patterns (see also Figure 4 for annual mean emissions). For example, in India a posteriori emissions are most pronounced over the Ganges valley, while a priori emissions are much more homogeneously distributed over the Indian subcontinent. In Africa, a posteriori emissions are extended over a large part of the tropics (while a priori emission are dominated by very strong wetland emissions from the Congo

Figure 2. Column-averaged CH_4 mixing ratios (XCH_4). (left) Revised SCIAMACHY retrievals (IMAP V5.0) versus (middle) TM5-4DVAR. Shown are 3 month composite averages. (right) The 3 month latitudinal average XCH_4 values (red: IMAP V5.0; blue: TM5-4DVAR) and the corresponding minimum and maximum values across the longitude.

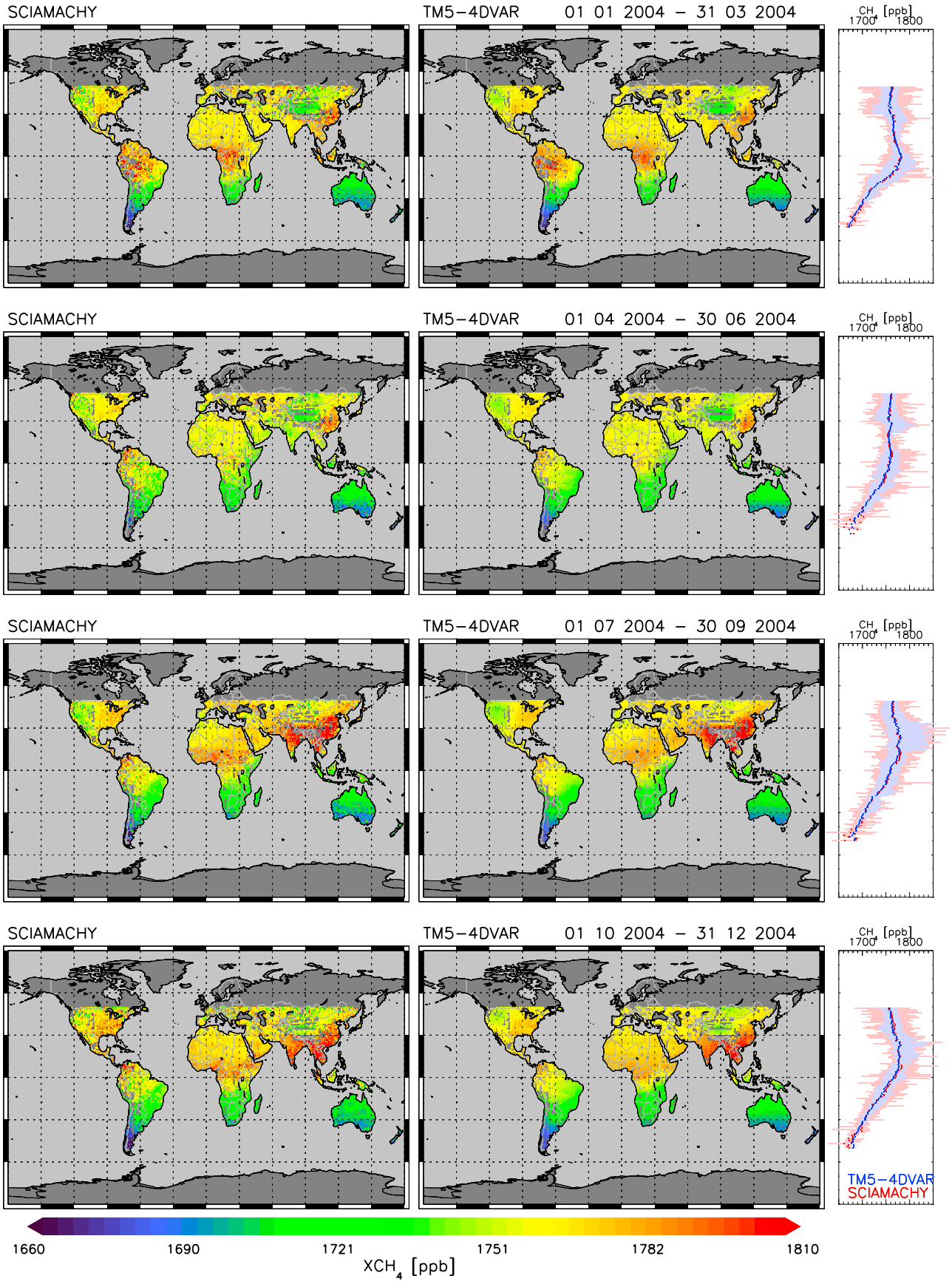
SCIAMACHY
TM5−4DVAR 01 01 2004 − 31 03 2004
CH4 [ppb]
1700
1800
SCIAMACHY
TM5−4DVAR 01 04 2004 − 30 06 2004
CH4 [ppb]
1700
1800
SCIAMACHY
TM5−4DVAR 01 07 2004 − 30 09 2004
CH4 [ppb]
1700
1800
SCIAMACHY
TM5−4DVAR 01 10 2004 − 31 12 2004
CH4 [ppb]
1700
1800
TM5−4DVAR
SCIAMACHY
1660
1690
1721
1751
1782
1810
XCH4 [ppb]

Figure 2

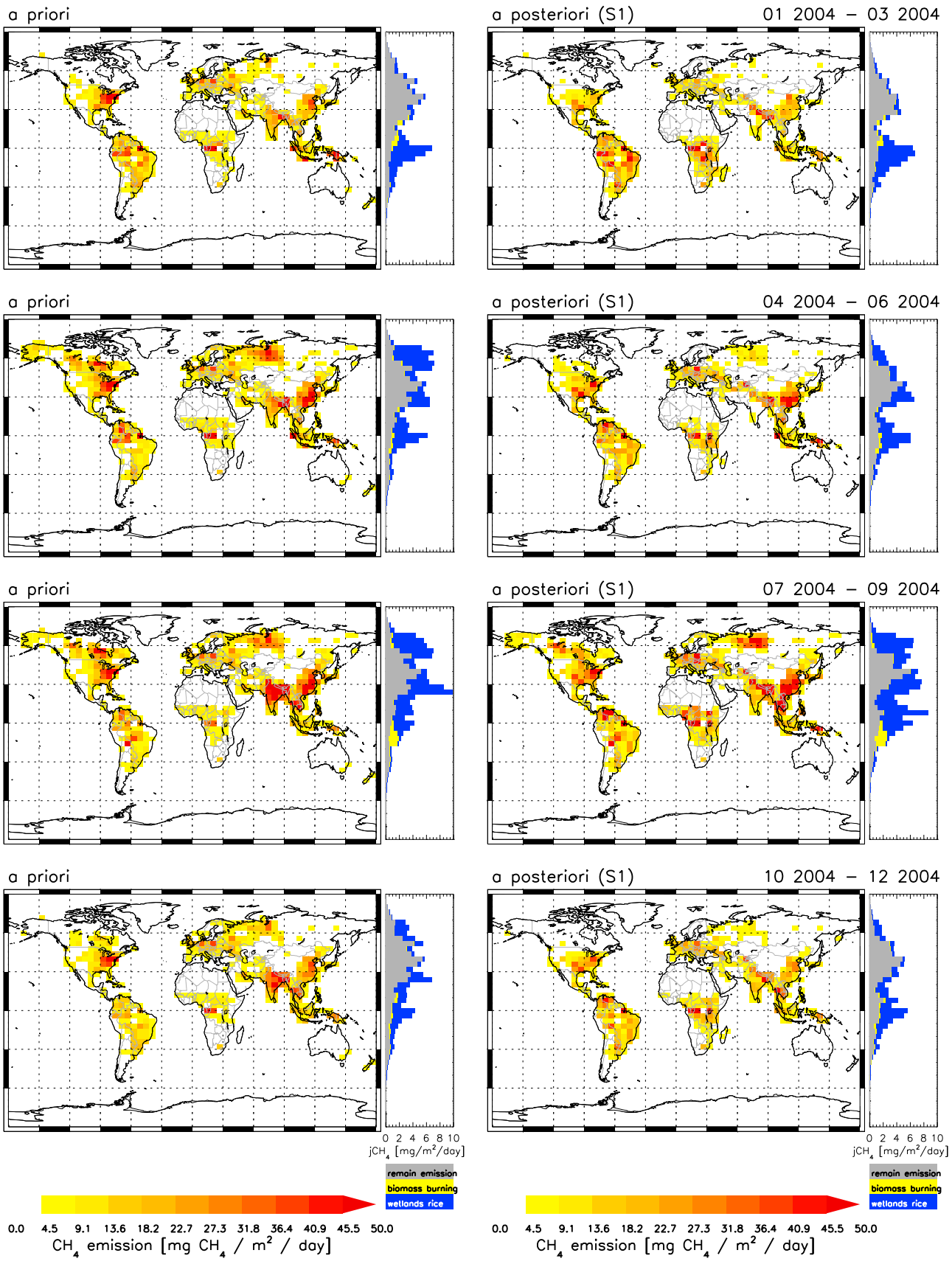

Figure 3. (left) A priori and (right) a posteriori emissions for reference inversion S1. Global distribution of total emissions (3 month average values) and partitioning among the three principal source categories which have been optimized in this study (3 month latitudinal averages).

Table 6. A Priori and a Posteriori Emissions for Major Global Regions and Global Totals[a]

Region	Source Category	A Priori	S1	S2	S3	S4	S5	S6	S7	S8
30°N−90°N	wetlands rice	68.9	55.1	58.1	58.8	58.4	54.5	55.3	57.2	
	biom. burning	1.7	1.6	1.6	1.7	1.6	1.6	1.6	1.5	
	remain. emis.	135.5	116.1	103.1	102.3	112.7	110.6	117.4	114.6	
	total	206.1	172.8	162.8	162.8	172.8	166.8	174.3	173.3	175.0
30°S−30°N	wetlands rice	163.5	185.0	224.6	204.2	186.4	189.6	198.1	182.9	
	biom. burning	18.3	20.1	18.5	21.5	20.5	21.3	22.7	21.9	
	remain. emis.	115.9	118.4	110.2	111.4	116.0	122.9	130.1	125.1	
	total	297.7	323.5	353.3	337.1	322.9	333.8	350.8	329.9	321.7
90°S−30°S	wetlands rice	2.3	2.5	1.8	2.1	2.3	2.5	3.0	2.5	
	biom. burning	0.1	0.1	0.1	0.1	0.1	0.1	0.1	0.1	
	remain. emis.	10.4	7.7	5.1	8.3	8.5	6.4	14.6	7.0	
	total	12.8	10.4	7.0	10.5	10.9	9.0	17.7	9.7	11.2
Globe	wetlands rice	234.6	242.7	284.5	265.1	247.2	246.7	256.3	242.7	
	biom. burning	20.1	21.7	20.2	23.3	22.3	22.9	24.4	23.5	
	remain. emis.	261.8	242.3	218.4	222.0	237.1	240.0	262.1	246.8	
	total	516.5	506.7	523.1	510.4	506.6	509.6	542.8	512.9	507.8
	photochemical sinks	520.3	519.3	519.5	519.5	519.3	519.7	541.4	519.5	519.1

[a]Units: Tg CH_4/yr.

basin), and in South America the inversion leads to larger increments in particular over Venezuela and Columbia, in the region of the Amazon delta, and along the east coast between 0 and 30°S.

4.1.2. Comparison of Reference Inversion S1 With Inversions Based on Previous SCIAMACHY IMAP V1.1 Retrievals (S2) and Based on Surface Stations Only (S3)

[42] Figure 4 shows annual total emissions for the reference inversion S1 and the sensitivity inversions S2 and S3 (including the a priori emissions which are identical for all 3 cases), and the differences between these inversions. The largest impact of the revision of the SCIAMACHY retrievals is apparent in the tropics, with significantly lower a posteriori emissions derived for the new retrievals, compared to the old IMAP V1.1 (sensitivity inversion S2). This is a direct consequence of the generally lower tropical XCH_4 values in the IMAP V5.0 retrievals (see *Frankenberg et al.* [2008a] and section 2.1). Summing up emissions from all tropical regions 'TR_sam', 'TR_afr', and 'TR_asi' (see Figure 1), yield annual total emission of 244 Tg CH_4/yr for sensitivity inversion S2, compared to 203 Tg CH_4/yr for the reference inversion S1 (see Table 7), i.e., a difference of 20%. The inversion based on NOAA stations only (sensitivity inversion S3) yields total tropical emissions close to those of reference inversion S1 (193 Tg CH_4/yr). An important difference between S1 and S3, however, is that the spatial patterns of the inversion increments in S3 largely follow those of the a priori emissions, because the remote surface stations mainly constrain the large-scale (continental scale) emissions. In contrast, the SCIAMACHY based inversions put significant constraints on the regional emission distributions over the continents. The total tropical emissions derived for inversions S1−S3 (Table 6) are very close to the first estimates presented by *Frankenberg et al.* [2008a], which were still based on the previous TM5-4DVAR system.

[43] While the observed XCH_4 can be reproduced rather well for the new retrievals (as shown in Figure 2), significant differences are apparent for the IMAP V1.1 (sensitiv-

Table 7. A Priori and a Posteriori Emissions for Tropical Regions and Asia[a]

Region	Source Category	A Priori	S1	S2	S3	S4	S5	S6	S7	S8
TR_sam	wetlands rice	43.1	54.1	71.6	54.4	56.3	55.6	59.1	50.5	
	biom. burning	4.6	5.3	5.0	5.6	5.5	5.4	6.2	5.5	
	remain. emis.	13.1	24.0	19.3	14.1	21.1	24.9	26.2	23.9	
	total	60.8	83.4	95.8	74.1	82.9	85.8	91.5	79.8	79.2
TR_afr	wetlands rice	23.8	37.1	54.1	41.4	37.4	37.9	40.0	37.3	
	biom. burning	5.9	7.4	6.0	7.9	7.5	8.1	8.5	8.2	
	remain. emis.	15.4	24.8	36.4	17.6	22.3	27.5	27.7	30.0	
	total	45.1	69.4	96.5	67.0	67.3	73.6	76.1	75.6	73.0
TR_asi	wetlands rice	34.9	36.6	36.2	36.2	36.4	39.0	42.0	39.2	
	biom. burning	3.1	3.4	4.1	3.4	3.5	3.6	3.7	3.7	
	remain. emis.	12.2	10.2	11.6	12.0	11.0	11.5	12.2	10.5	
	total	50.3	50.2	51.8	51.6	50.9	54.1	57.9	53.4	34.4
TR total	wetlands rice	101.8	127.9	161.9	132.0	130.1	132.5	141.1	127.0	
	biom. burning	13.7	16.1	15.0	17.0	16.5	17.1	18.3	17.5	
	remain. emis.	40.7	59.0	67.2	43.8	54.4	64.0	66.1	64.3	
	total	156.2	203.0	244.1	192.7	201.1	213.6	225.5	208.8	186.6
Asia	wetlands rice	74.0	69.2	76.8	84.5	68.5	69.8	69.2	72.2	
	biom. burning	3.6	2.9	2.9	2.7	3.0	3.1	3.0	3.2	
	remain. emis.	77.5	56.2	47.1	60.5	57.9	56.2	56.2	56.6	
	total	155.1	128.4	126.9	147.7	129.5	129.1	128.4	132.0	121.5

[a]Units: Tg CH_4/yr.

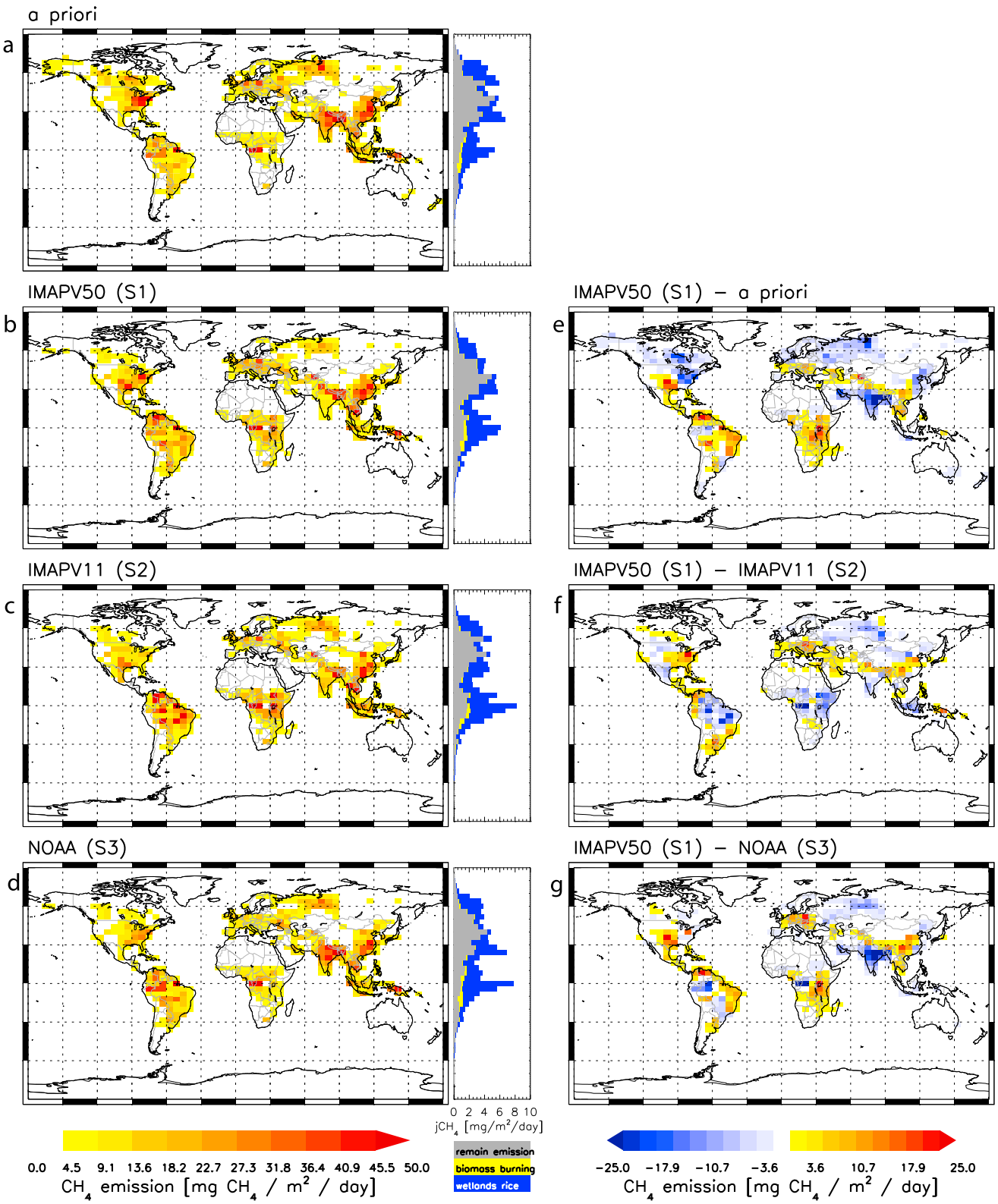

Figure 4. Annual mean emissions per 6° × 4° model grid cell. (a) A priori. A posteriori for inversions (b) S1, (c) S2, and (d) S3. Difference (e) S1 and a priori, (f) S1 and S2, and (g) S1 and S3.

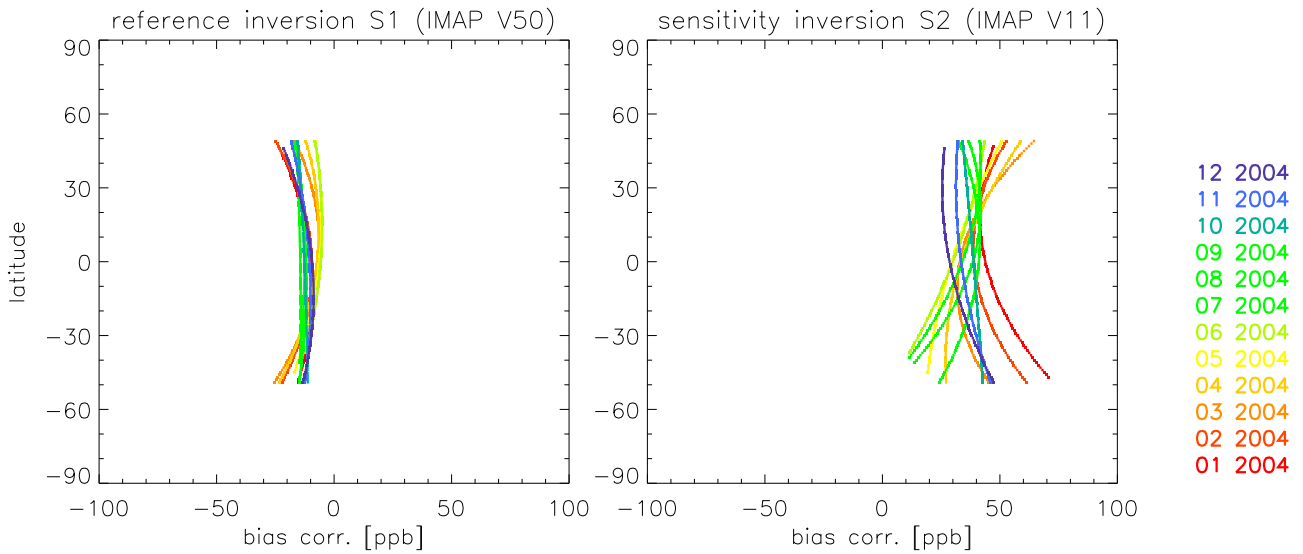

Figure 5. Derived latitudinal/monthly bias correction. (left) IMAP V5.0 (reference inversion S1). (right) IMAP V1.1 (sensitivity inversion S2).

ity inversion S2; see auxiliary material Figure S1).[1] In particular the very pronounced tropical enhancements of the IMAP V1.1 data set cannot be fully reproduced in the simulations despite higher tropical emissions derived in sensitivity inversion S2. This is clearly evident in the latitudinal XCH_4 averages with differences of up to 20 ppb between IMAP V1.1 and TM5 in the tropics (Figure S1).

[44] Allowing for potential latitudinal and seasonal biases of the retrievals, both IMAP V1.1 and IMAP V5.0 can be reconciled with the surface measurements. However, using the new retrievals (reference inversion S1), the calculated bias correction is significantly smaller than that calculated for the IMAP V1.1 based inversion (sensitivity inversion S2), as illustrated in Figure 5: The latitudinal dependence of the bias corrections for S1 is typically only one third of that calculated for S2. Furthermore, a posteriori simulations of reference inversion S1 agree better with measurements at the tropical sites (RPB, CHR, SEY, ASC and SMO) than those of sensitivity inversion S2 (see auxiliary material Figure S3).

[45] This altogether clearly demonstrates the major progress achieved with the new retrievals, leading to an overall much better consistency with the high-accuracy surface measurements. This is also further supported by independent validation data (see section 4.2).

[46] The large tropical XCH_4 derived in the previous IMAP V1.1 retrievals seemed to support the hypothesis of significant CH_4 emissions from plants under aerobic conditions proposed by *Keppler et al.* [2006], as further evaluated by *Houweling et al.* [2008]. However, the study of *Keppler et al.* [2006] was questioned by *Dueck et al.* [2007], who did not find any evidence for substantial CH_4 emissions of plants under aerobic conditions. Nevertheless, later studies suggest that breakdown of detached plant material under high UV radiation may release some CH_4 [*Vigano et al.*, 2008], but the importance of this process for the global CH_4 budget is probably rather small [*Nisbet et al.*, 2009]. *Nisbet et al.* [2009] discuss also the role of transport of CH_4 dissolved in soil water through plants, which may partly explain the experiments of *Keppler et al.* [2006]. Such processes, however, are mainly important for wetland plants (for which they are usually covered by the emission inventories), and should play only a small role for plants living on dry land [*Nisbet et al.*, 2009]. Our study suggests that wetlands play a dominant role for the tropical enhancements observed by SCIAMACHY, but clearly does not rule out additional sources which were not considered (e.g., additional plant emissions). Furthermore we note that the inversions do not provide direct information on the source categories. Only applying some a priori knowledge on the likely spatial and temporal distribution of the different source categories allows the attribution of the derived emissions to these categories in the inversion.

4.1.3. Sensitivity Experiments

[47] Further experiments have been performed to investigate the sensitivity of the inversion results to critical assumptions and settings of the 4DVAR system (Figure 6 and Tables 5, 6, and 7). The reduction of the horizontal correlation length from 500 to 100 km (sensitivity inversion S4) results in slightly more pronounced emission hot spots, but the overall impact on the derived spatial patterns is rather small, and the totals for the major global regions listed in Tables 6 and 7 remain very close to our reference inversion S1.

[48] In sensitivity inversion S5, only a monthly constant bias is allowed instead of the standard second order polynomial as function of latitude. The resulting tropical emissions are only slightly higher (~5%) compared to our reference inversion, and the impact on the derived spatial emission patterns is relatively small. Furthermore, both the SCIAMACHY data and the surface observations can still be reproduced relatively well (see auxiliary material Figures S2 and S3). The calculated bias is relatively constant through-

[1] Auxiliary materials are available with the full article. doi:10.1029/2009JD012287.

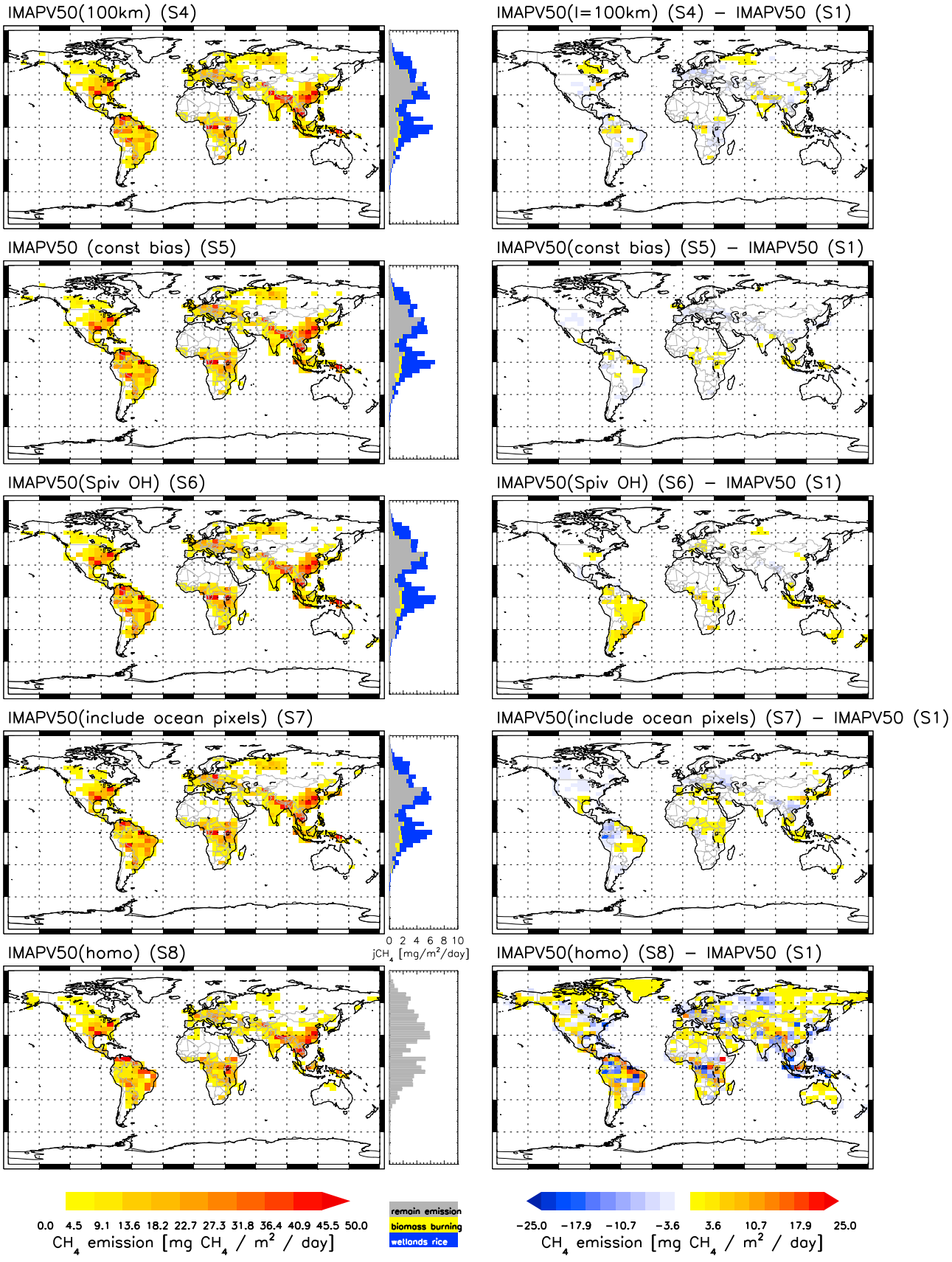

Figure 6. (left) Annual mean emissions derived in various sensitivity experiments and (right) difference from reference inversion S1.

out the year (-13.2 ± 2.5 ppb). While the correction of the large biases of the previous retrievals was considered an issue of major concern with a potential significant impact on the derived emissions [*Meirink et al.*, 2008a], the sensitivity inversion S5 suggests that the bias correction is now much less critical for the new retrievals.

[49] The use of the OH fields from *Spivakovsky et al.* [2000] in sensitivity inversion S6 results in significantly higher derived global total emissions (~7%), mainly attributed to the tropics. These higher emissions are a direct consequence of the higher OH values (compared to the standard fields from TM5 used in all other inversions), which need to be balanced in the inversion. However, the total photochemical sinks in S6 are only 4% higher than in the reference inversion i.e., sources and sinks are almost in balance in this case resulting in somewhat better agreement with observations in the extratropical SH toward the end of 2004 (see auxiliary material Figure S3). The difference of ~4% for the total photochemical sinks is smaller than the currently assumed uncertainty and potential interannual variability of global OH (~10%) [*Bousquet et al.*, 2005; *IPCC*, 2007; *Krol and Lelieveld*, 2003; *Rigby et al.*, 2008]. Hence, the real uncertainties of derived emissions due to OH are likely to be even larger than the difference between sensitivity inversion S6 and the reference inversion.

[50] In sensitivity inversion S7 we also included the SCIAMACHY pixels over the ocean. The largest difference in derived emissions is apparent in tropical South America, with higher emissions at the east coast and lower emissions at the west coast. At the same time, the XCH_4 residuals (i.e., $XCH_{4\ TM5} - XCH_{4\ SCIAMACHY}$) show some tendency to positive values over the ocean, and to negative values over land close to the coastline (not shown), pointing to a potential small land-ocean bias of the SCIAMACHY retrievals, which could lead to systematic errors in the inversion. For marine air masses arriving at the east coast (trade wind zone), a bias toward lower XCH_4 values for the measurements over the ocean is compensated in the inversion by enhancing emissions along the coast, while for air masses leaving the continent at the east coast the opposite effect occurs. Further investigation of this systematic effect and its dependence on the retrieval selection criteria will be necessary to make better use also of the ocean pixels. In this study the ocean pixels are generally excluded (except for this sensitivity experiment S7).

[51] Finally, we performed a further sensitivity experiment to explore the impact of the applied a priori emission inventories. In the standard setup the spatial patterns of the a priori inventories strongly constrain the solution space, since uncertainties of the grid cell emissions are specified as percentage of the emissions. This implies that model grid cells with low a priori emissions can usually not turn into grid cells with very high emissions, while for emission hot spots in the a priori inventories a relatively small fractional increase or decrease may have a large regional impact, leading to a clear tendency of the inverse modeling system to ''optimize'' such hot spots. At the same time it is recognized that existing bottom-up inventories have clear deficiencies regarding their spatial and temporal emission patterns. This is in particular the case for source categories with larger spatial and temporal variability, such as wetlands. On the other hand, the almost global coverage of the SCIAMACHY observations provides strong constraints, which may allow at least for some regions to derive emissions without the use of a priori emission inventories with detailed spatial and temporal disaggregation. For sensitivity inversion S8 we constructed an alternative a priori emission inventory in which emissions are distributed homogeneously over land (except Antarctica), using an annual total of 500 Tg CH_4/yr. In addition we account for emissions over the ocean and distribute an assumed total of 17 Tg CH_4/yr over the ocean. The a priori uncertainty of these homogeneous emissions have been set to a very large value (300%) to give the inverse modeling system a large degree of freedom to optimize the spatial emission patterns. Figure 6 shows that the derived emission patterns for this sensitivity inversion agree remarkably well with those from our reference inversion S1 for several regions. This is particular the case for emissions in India, China, and South East Asia, which are well constrained by the SCIAMACHY retrievals due to the large observed XCH_4 gradients. Also for the United States a very good agreement in the spatial patterns is visible. Major differences to the reference inversion S1 are apparent in particular for Western tropical Africa (with significantly lower emissions especially over the Congo basin for sensitivity inversion S8) and over tropical South America, where higher emissions are attributed along the East coast in sensitivity inversion S8, but less in the inner part of the Amazon basin. These discrepancies point to some potential deficiencies in the spatiotemporal patterns of the applied bottom-up inventories. At the same time, however, it is clear that this 'free inversion' of sensitivity inversion S8 is more sensitive to potential systematic errors in the retrievals (and modeling errors), as it is not guided by the a priori information about the expected spatial and temporal patterns. The free inversion appears to be successful in deriving very low emissions over the Sahara, Australia and Greenland, consistent with our standard a priori inventory (Figure 4).

4.2. Validation of Assimilated 3D CH_4 Fields

[52] A comprehensive validation of optimized 3D fields (inversions S1, S2, and S3) has been performed using measurements from regular NOAA ocean transects and aircraft profiles, as well as stratospheric samples from balloon soundings (University Frankfurt, Germany). These additional observational data sets were generally not used in the inversions; hence they serve as independent validation of simulated 3D mixing ratios.

4.2.1. Ocean Transects

[53] The oceanic transects are depicted in Figure 7. The observed latitudinal gradient and its seasonal variation are reproduced very well by the model simulations, demonstrating the overall very good simulation of the marine background mixing ratios. This good agreement was expected, since all inversions use the measurements from the global NOAA monitoring sites. Therefore, the surface mixing ratios over the remote ocean are well constrained by the observations (observed and simulated mixing ratios at the NOAA sites are shown in auxiliary material Figure S3). In general, model simulations of the oceanic transects are very close to each other for the different inversions. A striking difference, however, is the clear tendency to higher values (~10 ppb) for sensitivity inversion S2 in the Atlantic

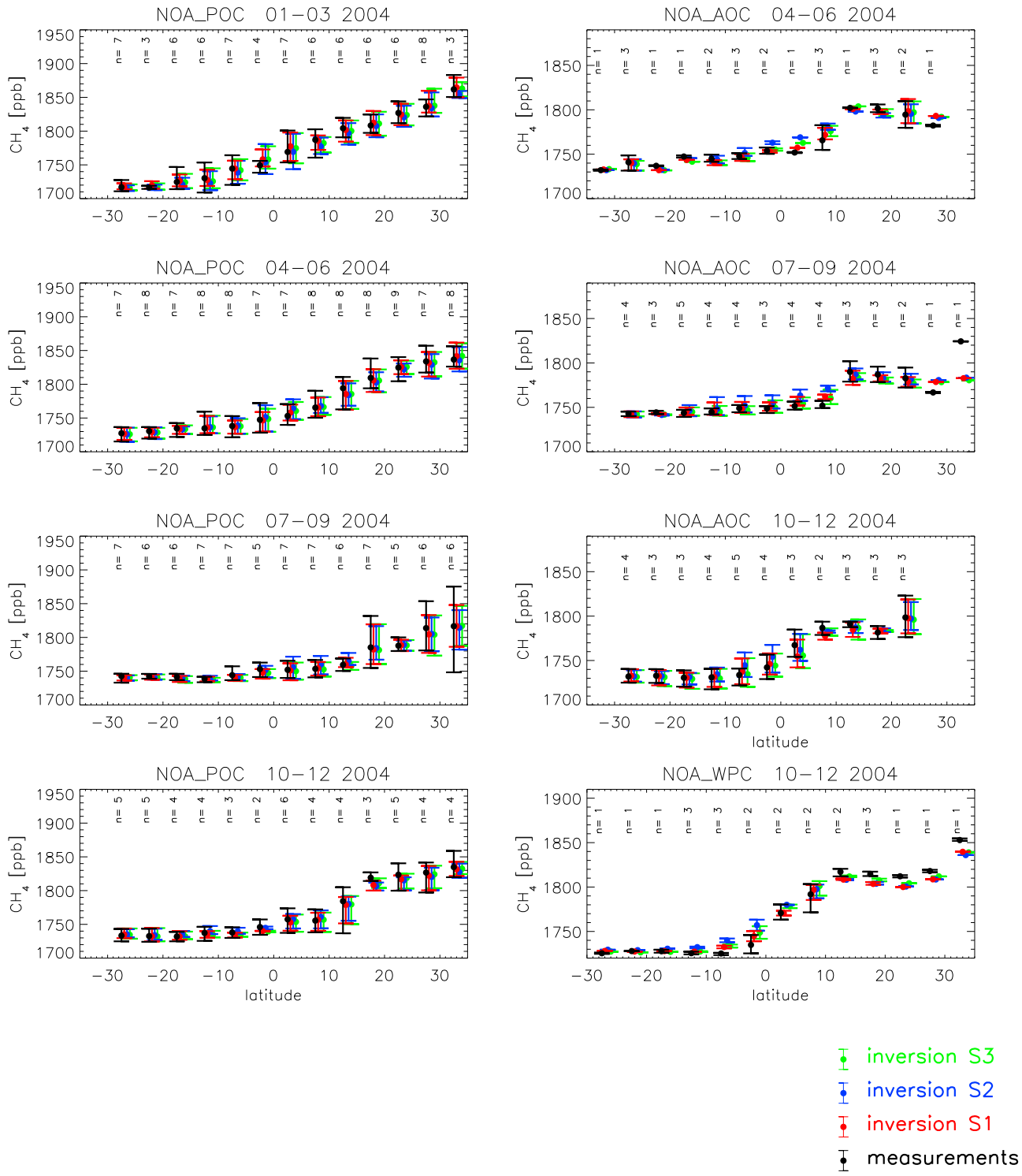

Figure 7. NOAA measurements from commercial ships used for validation. Three month composite averages for 5° latitude bins are shown for the POC, AOC, and WPC transects (measurements and model simulations for inversions S1−S3; model simulations are sampled at the same time as the measurements). The vertical bars indicate the minimum and maximum values, and the listed values of n are the number of available observations within each 3 month 5° latitude bin.

Ocean (AOC) and West Pacific (WPC) transects close to the equator, while the model simulations of the other inversions match the observations much better. These higher mixing ratios are the result of the ∼20% higher tropical emissions of sensitivity inversion S2, resulting in a less consistent picture with the oceanic transect validation data.

4.2.2. Aircraft Profiles

[54] In contrast to surface mixing ratios, the simulated vertical gradients are much less constrained by the obser-

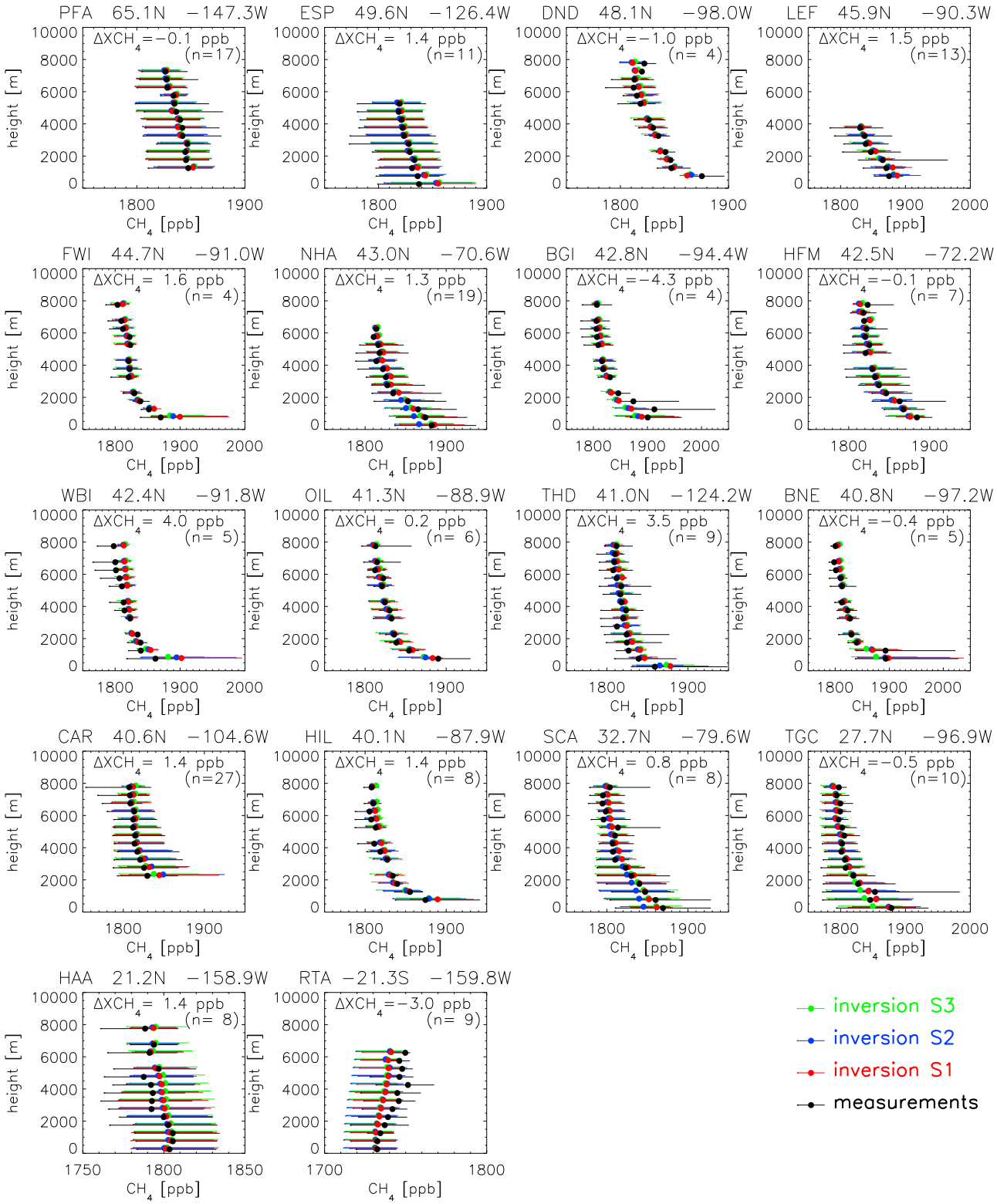

Figure 8. Aircraft profiles used for validation. Average values for all profiles taken in year 2004 (measurements and model simulations for inversions S1−S3; model simulations are sampled at the same time as the measurements). The horizontal bars indicate the minimum and maximum values, n is the number of available profiles at each site, and ΔXCH_4 is the difference in column-averaged mixing ratio arising from the difference between observed and simulated mixing ratios over the altitude range of the observations (evaluated for reference inversion S1).

vational data, and are largely determined by the vertical mixing of the transport model. Validation of the simulated vertical gradients is essential to investigate the model's capability to simulate the column-averaged mixing ratios observed from SCIAMACHY. Furthermore, validation of vertical mixing is very important to evaluate potential systematic errors in the derived emissions [*Peters et al.*, 2007; *Stephens et al.*, 2007]. In Figure 8 we present the comparison of model simulations with aircraft profiles, showing overall good agreement. Most of the profiles are over the United States, covering the altitude range between ~1 and ~8 km. Typical gradients are on the order of 50–100 ppb between the boundary layer and the upper free troposphere which is generally well captured by the model simulations. Model simulations for the different inversions are very close to each other, except for small differences in the boundary layer for some profiles, reflecting small differences in the derived emissions. Integrated over the whole altitude range of the measurements, the difference between model simulations and measurements translates into a maximum difference in column-averaged mixing ratios of ~4 ppb, but is in most cases much smaller (see Figure 8).

[55] For the subtropical site HAA (21.2°N) model simulations are somewhat higher (~10 ppb) than observations in the free troposphere (between ~3 and ~5 km), while they are lower at RTA (21.3°S) between ~2 and 6.5 km. Hence the simulated latitudinal gradient across the equator in the free troposphere is smaller than observed. Despite the relatively small integrated effect (ΔXCH_4 = 1.4 ppb (HAA) and ΔXCH_4 = −3.0 ppb (RTA)) this discrepancy could be an indication that interhemispheric exchange might be too weak in TM5, consistent with the observation that simulated SF_6 mixing ratios in the SH are slightly smaller than measurements [*Bergamaschi et al.*, 2006; *Peters et al.*, 2004]. However, the 3D interhemispheric mixing time derived from SF_6 simulations of 10.4 months [*Bergamaschi et al.*, 2006] is well within the range derived in the TransCom2 intercomparison [*Denning et al.*, 1999].

4.2.3. Validation of Stratospheric CH_4 Mixing Ratios

[56] In addition to vertical profiles in the troposphere, stratospheric mixing ratios also contribute significantly to the XCH_4 derived in the SCIAMACHY retrievals, although the averaging kernel is typically smaller in the stratosphere [*Frankenberg et al.*, 2006]. In our previous analysis of the IMAP V1.1 retrievals [*Bergamaschi et al.*, 2007] we compared simulated CH_4 mixing ratios in the stratosphere with measurements from HALOE/CLAES [*Randel et al.*, 1998], concluding that potential deficiencies of the modeled stratosphere are likely to have only a very small impact on simulated XCH_4 (except some potential constant offset, and except the polar vortices). We repeated this comparison with the model fields of this study, basically confirming the earlier conclusions. However, it cannot be ruled out that the HALOE/CLAES data themselves may have some bias, and an intensive intercomparison including various further remote sensing data (including ACE-FTS, MIPAS, and ground-based FTIR) identified significant biases among these different data sets [*De Mazière et al.*, 2008]. Therefore, we use high-accuracy measurements of air samples taken from balloon soundings for further validation of our model fields. These measurements can be assumed to be unbiased, but are sparser in space and time than the remote sensing data. For that reason we use all measurements made between 1999 and 2005 for comparison with the model simulations of year 2004. Model values are sampled at the same day of the year (and time) as the measurements, but no correction was made for interannual variations or trends. Figure 9 depicts this comparison for 3 month 5° latitude bins. Over the tropics, model simulations match the observations almost perfectly. Integrated over the altitude range of the measurements the difference between model simulations and observations translate into a difference of ΔXCH_{4eff} = 0.0 ppb (taking into account also the SCIAMACHY averaging kernels). In the midlatitudes (40–45°N) some differences are apparent in the exact shape of the profile (in particular for the 3rd and 4th quarter of the year), but the integrated difference remains relatively small with derived ΔXCH_{4eff} values between 2.9 and 7.8 ppb. In contrast, large differences are visible at high latitudes (65–70°N), particularly in the first quarter of the year due to the polar vortex which is not well reproduced in the model, resulting in a ΔXCH_{4eff} value of 26.0 ppb. Since no SCIAMACHY measurements are available at high latitudes during this period, this mismatch would not be relevant. However, in the 2nd quarter the high latitude profile also shows a significant CH_4 depletion around 20 km with a ΔXCH_{4eff} value of 12.6 ppb. This feature is caused by remnants of the polar vortex, and could be reproduced by the Chemical Lagrangian Model of the Stratosphere (CLaMS) [*Grooß et al.*, 2008]. Since the measurements are from a single profile only, taken at a different year than the TM5-4DVAR model simulations (B41, 9 June 2003; see Table 3) they represent a specific synoptic situation, which might not be representative for other years. Nevertheless, they demonstrate the potential systematic error arising from such structures related to the polar vortex. In order to minimize the impact of model deficiencies in the stratosphere at high latitudes, we therefore chose to generally exclude the high-latitude SCIAMACHY measurements in this study, and use only the data between 50°S and 50°N. An additional advantage of this restriction is that the data coverage is more continuous in time, reducing a potential seasonal bias in the inversion due to seasonally varying availability of observations. The difference in ΔXCH_{4eff} between midlatitudes and tropics (2.9...7.8 ppb) is close to the variation of the derived bias correction between these latitudes (see Figure 5), suggesting that significant parts of the derived bias corrections might be attributable to the deficiencies of the model stratosphere. We note, however, that our analysis is limited by the fact that we use measurements from different years than the model simulations. Hence interannual variations and trends in stratospheric CH_4 (which are not considered in our analysis) may also affect the derived ΔXCH_{4eff} values [*Rohs et al.*, 2006].

4.3. Regional Inversions

[57] In the following we present a more detailed analysis for South America, Africa, and Asia, based on additional inversions using the 1 × 1 zoom over these regions (see Table 5).

4.3.1. South America

[58] Figure 10 depicts observed and simulated XCH_4, along with a posteriori emissions for inversion S1Z. Overall, the spatial patterns in observed XCH_4 and their seasonal

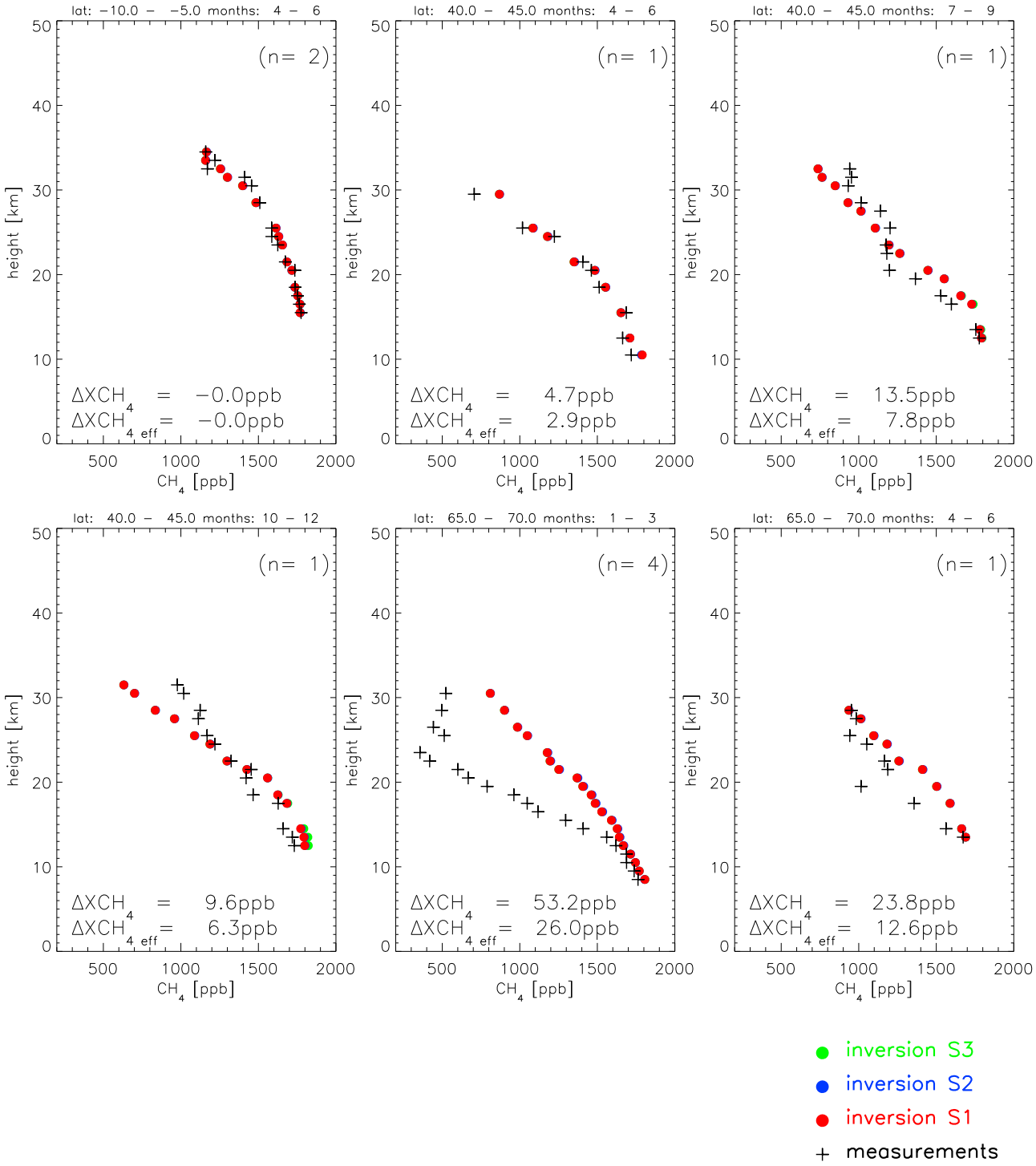

Figure 9. Balloon-borne observations and simulations in the stratosphere (measurements and model simulations for inversions S1−S3; note that model simulations are virtually identical for all three cases). n is the number of profiles within each 5° latitude/3 month bin. The individual profiles used are listed in Table 3. ΔXCH_4 is the difference in column-averaged mixing ratio arising from the difference between observed and simulated mixing ratios over the altitude range of the observations (neglecting the averaging kernels), evaluated for reference inversion S1. ΔXCH_{4eff} takes into the account the SCIAMACHY averaging kernels.

variation are well reproduced by the model. Large emissions are attributed to the major wetland areas, in particular to the Amazon basin, but also to the Orinoco River plain (Venezuela), the Llanos de Mojos (Bolivia; influx area of Madeira river), the Pantanal region, and the Paraná River floodplain. The wetlands show a pronounced seasonality with largest emissions during the wet season (January−March). During the SH dry season (July to September) significant

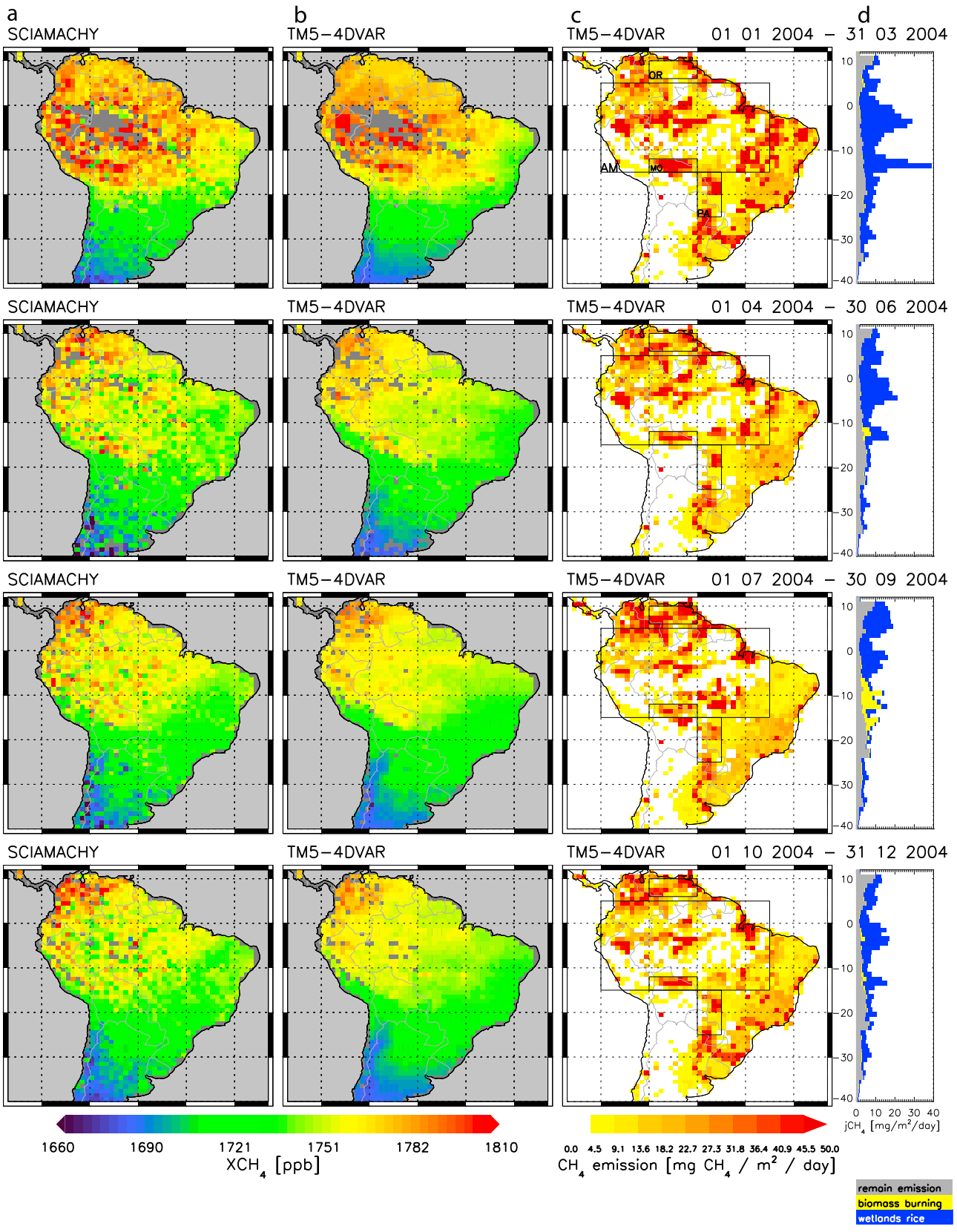

Figure 10. Column-averaged CH_4 mixing ratios (XCH_4) over South America. (a) SCIAMACHY retrievals (IMAP V5.0). (b) TM5-4DVAR. (c) Retrieved emissions per $1^\circ \times 1^\circ$ grid cell. (d) Latitudinal average emission (average over longitude range of zoom region (as displayed in Figures 10a−10c)), showing also the contributions from the three principal source categories optimized in the inversions.

Table 8. A Priori and a Posteriori Emissions for Various Wetland Regions in South America[a]

Region	Source Category	A priori	S1Z	S2Z	S3Z	S8Z	M2004
Amazon	wetlands rice	34.3	40.2	52.0	42.0		29.3
	biom. burning	4.3	4.1	4.3	5.0		
	remain. emis.	5.5	7.7	7.2	6.0		
	total	44.2	52.0	63.5	53.0	47.5	
Llanos de Mojos	wetlands rice	1.3	5.2	6.1	3.4		2.9
	biom. burning	0.6	0.4	0.4	0.6		
	remain. emis.	0.1	0.0	0.0	0.0		
	total	1.9	5.6	6.5	4.0	2.9	
Orinoco	wetlands rice	2.5	4.5	5.4	3.0		3.3
	biom. burning	0.1	0.1	0.1	0.1		
	remain. emis.	1.1	1.6	1.6	0.9		
	total	3.6	6.1	7.1	4.0	5.8	
Pantanal	wetlands rice	2.0	2.8	3.2	3.0		3.3
	biom. burning	0.1	0.3	0.2	0.2		
	remain. emis.	0.9	1.0	0.8	0.9		
	total	3.1	4.1	4.2	4.0	3.4	

[a]Units: Tg CH_4/yr. Estimates for wetland emissions by *Melack et al.* [2004] are given in the M2004 column.

emissions are attributed to biomass burning between 5 and 15°S. Furthermore, anthropogenic emissions play an important role, in particular over Venezuela, Columbia, and South Eastern Brazil.

[59] Table 8 lists the emissions for major wetland areas in South America, derived for the 4 inversions run with zooming over South America (see Table 5). The use of the IMAP V5.0 retrievals (inversion S1Z) results in ~20% lower emissions over the Amazon compared to the previous IMAP V1.1 data set (sensitivity inversion S2Z) and is rather close to the value derived for sensitivity inversion S3Z (using only the NOAA observations), hence largely reflecting the differences for the total tropical emissions as discussed in section 4.1.2 based on the global coarse resolution inversions. The 'free inversion', sensitivity inversion S8Z, yields only slightly lower values for the Amazon (47.5 Tg CH_4/yr) compared to S1Z (52.0 Tg CH_4/yr).

[60] Based on microwave remote sensing and an extensive set of flux measurements available from the literature, *Melack et al.* [2004] estimated the total emissions from wetlands in the Amazon basin to be 29.3 Tg CH_4/yr. We note, however, that the definition of the Amazon region is somewhat different in their study (and could not be exactly reproduced from the information given in their paper), adding some uncertainty to the comparison with the values derived in our study.

[61] Inversion S1Z yields 40.2 Tg CH_4/yr for the category 'wetland and rice' (with rice paddies playing only a minor role in this region according to our a priori inventories (<1% of 'wetland and rice')), i.e., ~30% higher than the *Melack et al.* [2004] estimate, which, given the overall uncertainties of the bottom-up and top-down estimates (including the correct attribution to the different source categories), uncertainties from the exact area used for the comparison, and potential interannual variability of wetland emissions, is considered to be broadly consistent. Sensitivity inversion S2Z, on the other hand yields substantially higher emissions for the Amazon region (52.0 Tg CH_4/yr for category 'wetland and rice', i.e., 77% higher than the *Melack et al.* [2004] estimate).

[62] As already seen from the global coarse resolution inversions (section 4.1.2) the use of SCIAMACHY data results in significant changes in the smaller-scale emission patterns, compared to the inversion based on the NOAA data only. This is in particular noticeable for the Llanos de Mojos and the Orinoco River plain, for which inversion S1Z yields significantly higher emission than S3Z (~40–50%) (see Table 8). The emissions attributed to 'wetlands and rice' in S1Z are ~79% higher for the Llanos de Mojos and ~36% higher for the Orinoco River plain than the estimates of *Melack et al.* [2004], while the corresponding emissions derived in S3Z are very close to the Melack et al. estimates. Beside the use of the observational data, the emissions derived in the inversions depend significantly on the use of the a priori inventory. This is in particular the case for the Llanos de Mojos, with the 'free inversion' S8Z yielding only ~52% (2.9 Tg CH_4/yr) of the total emissions derived in inversion S1Z (5.6 Tg CH_4/yr). For the Pantanal region, the differences among the different inversions are generally rather small, and the emissions attributed to 'wetland and rice' are very close (~10%) to the *Melack et al.* [2004] estimates. As for the Amazon, rice cultivation plays an only minor role (<1% according to our a priori inventories) in these other wetland regions.

[63] Finally, we compare simulated mixing ratios with measured aircraft profiles for the 3 South American sites Santarem, Manaus, and Fortaleza (Figure 11). The upper panel shows this comparison using all available observations over the period 2000–2005 (with model values from 2004, but taken at the same day of the year (and time), and interannual variations of the observations corrected using measurements at the NOAA site Ascension Islands (ASC) as reference [see also *Meirink et al.*, 2008a], while the lower panel shows the comparison using only the observations of year 2004. Observed mixing ratios in the free troposphere are matched very well for all inversions which use either the new SCIAMACHY retrievals (S1Z and S8Z) or the NOAA surface measurements only (S3Z), while sensitivity inversion S2Z (based on the old IMAP V1.1 retrievals), results in higher mixing ratios. This, again, is a strong indication that sensitivity inversions S2 and S2Z overestimate the tropical emissions, leading to a significant enhancement of CH_4 mixing ratios in the free troposphere, which is not visible in the measurements. The comparison is more difficult to interpret in the boundary layer, since simulated mixing ratios strongly depend on the emissions of the local model

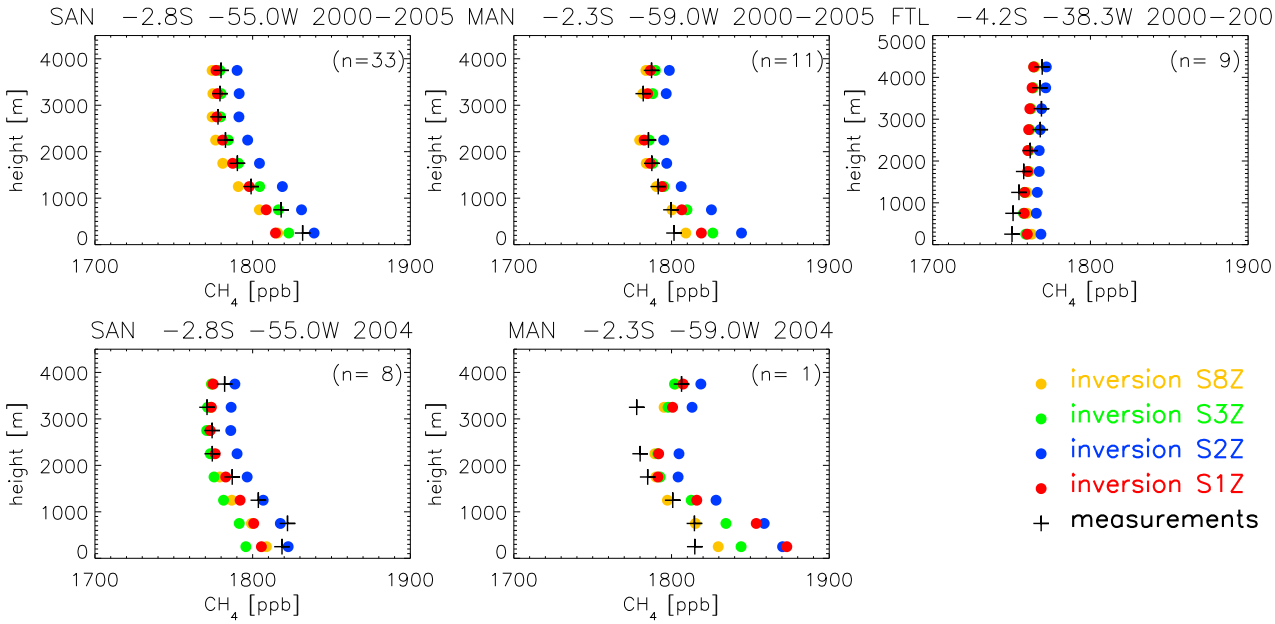

Figure 11. Aircraft profiles over South America for the sites Santarem (SAN), Manaus (MAN), and Fortaleza (FTL). Comparison of measurements with model simulations for inversions S1Z, S2Z, S3Z, and S8Z. (top) All measurements during the period 2000–2005 (see text for application of small correction for interannual variability), compared with model simulations of year 2004. (bottom) Measurements and model simulations of year 2004 only. Here n is the number of available profiles.

grid cell and subgrid scale variability of emissions has to be taken into account. While simulated mixing ratios in the boundary layer are broadly consistent with observations at Santarem, they are generally higher at Manaus. Interestingly, S8Z yields the best agreement, since emissions for the Manaus grid cell are lower in this sensitivity inversion compared to inversions S1Z, S2Z, and S3Z which are 'guided' by large a priori emissions in this grid cell. At Fortaleza simulated mixing ratios in the boundary layer are generally higher than observed, most likely because measurements mainly sample air coming from the Atlantic Ocean, while the simulations are influenced by the emissions of the whole model grid cell, as frequently observed at sites at the land-sea border [*Peters et al.*, 2004].

4.3.2. Africa

[64] Similar to South America, tropical Africa is characterized by strong seasonal variations of emissions from wetlands and biomass burning following the wet and dry season (Figure 12). Overall, the spatial patterns of observed XCH_4 and their seasonal variation are well reproduced in the simulations. In the third quarter of the year, however, simulations show a stronger enhancement in XCH_4 over the Congo basin than the SCIAMACHY observations. Obviously, the a posteriori emissions have been strongly guided by the very pronounced wetland emissions from the Congo basin in the bottom-up wetland inventory, while the SCIAMACHY measurements suggest a more homogeneous distribution over a larger area.

[65] The inversion leads to a significant increase of emissions around Lake Victoria, a feature which is also clearly seen in the global coarse resolution inversions (Figure 3). Furthermore, large emissions are attributed to the swamp area of the Upper Nile in Sudan, the wetlands in Southern Chad and the Niger delta, especially during the wet season (mainly third quarter of the year). Considerable emissions over the Niger delta, however, persist during the remainder of the year, although at lower intensity, derived from significant XCH_4 enhancements over this region discernible throughout the year.

[66] A prominent emission hot spot is visible around Johannesburg, South Africa, attributed according to the EDGAR database mainly to coal mining in this area. It is interesting to note that this emission peak can also be seen in the coarse resolution free inversion (sensitivity inversion S8, Figure 6), i.e., it is identified from the SCIAMACHY observations even without a priori information (but attributed a lower intensity than in reference inversions S1/S1Z).

4.3.3. Asia

[67] Observed and simulated XCH_4 over Asia are shown in Figure 13, along with the derived emissions. This region is strongly influenced by emissions from rice cultivation with a very pronounced seasonality. In particular during the third quarter of the year a prominent enhancement in XCH_4 is visible over India, Bangladesh, South East China, and Mainland Southeast Asia, largely attributed to rice emissions in this area. A major difference from the applied a priori emission inventory is the earlier end-of-season decline of the rice emissions in inversion S1Z, resulting in significantly lower rice emissions in the last quarter of the year. This change in the seasonality is also clearly visible in the various coarse resolution inversions that use the SCIAMACHY observations (see e.g., Figure 3), and had been observed already in our previous studies based on the IMAP V1.1 retrievals [*Bergamaschi et al.*, 2007; *Meirink et al.*, 2008a].

[68] Beside rice paddies, further anthropogenic emissions play an important role in this densely populated area, in particular emissions from ruminants and waste, and coal

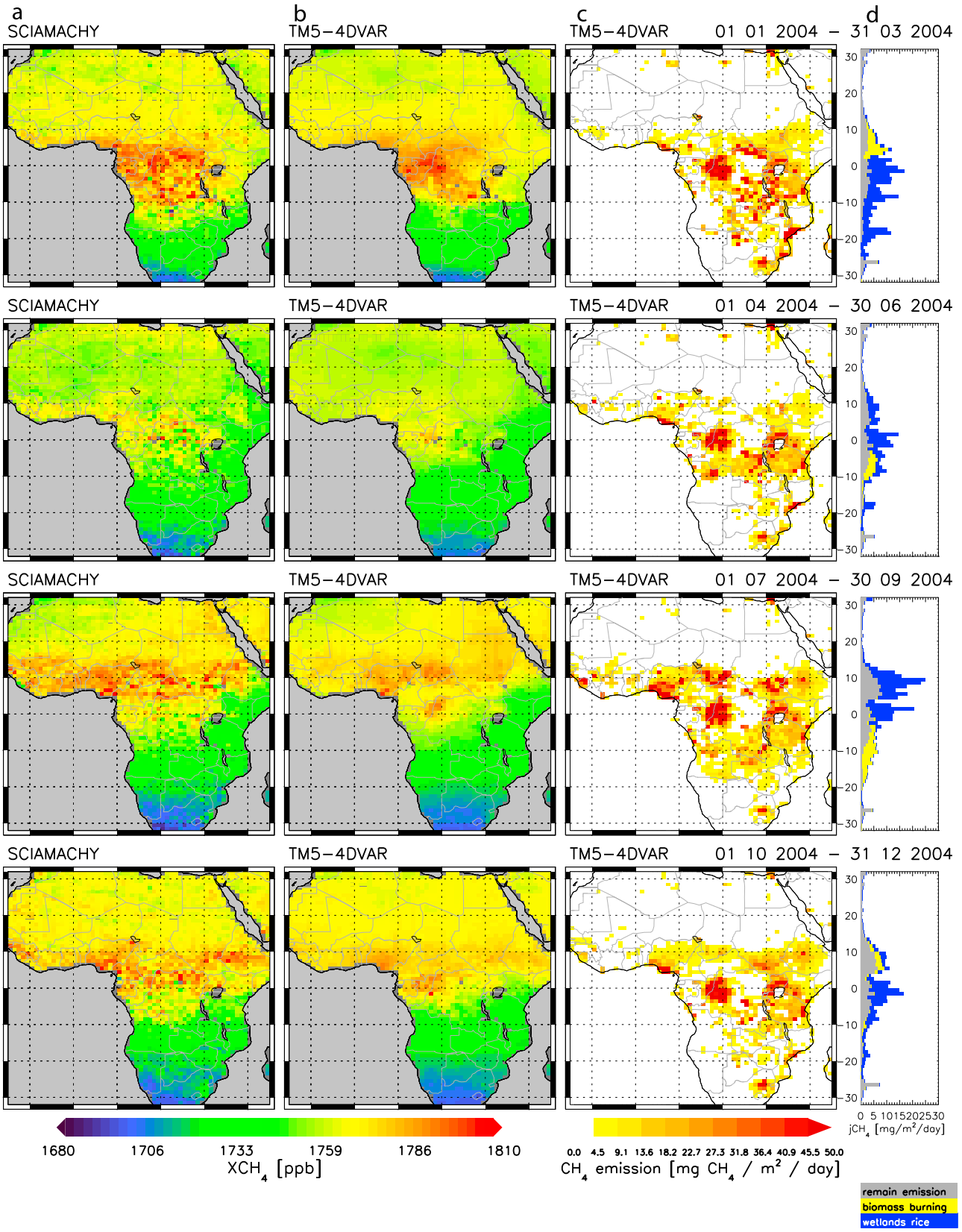

Figure 12. Same as Figure 10 but for Africa.

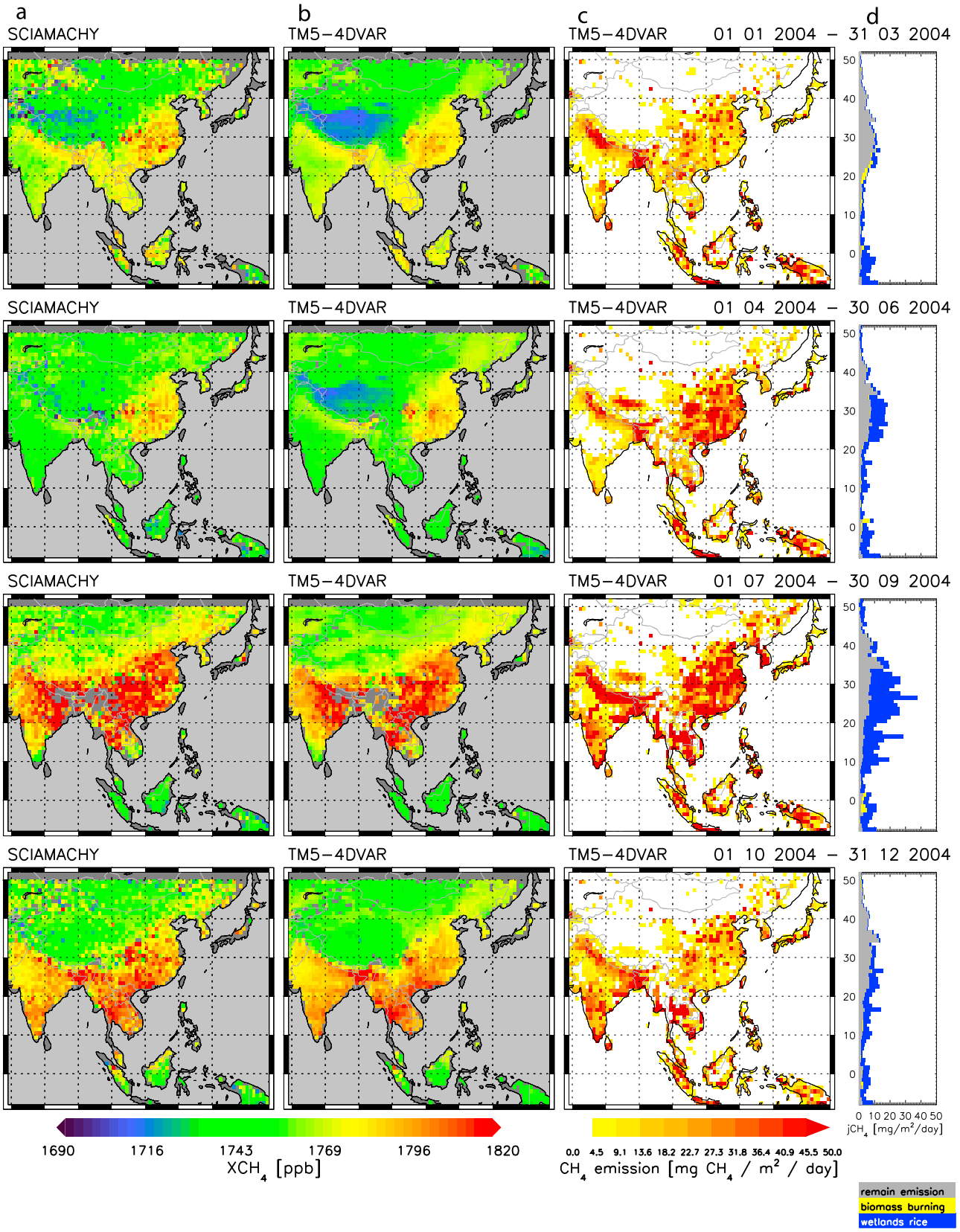

Figure 13. Same as Figure 10 but for Asia.

mining especially in China. However, all inversions attribute somewhat lower emissions (~22–27%) to our category 'remaining emissions' compared to the a priori estimates (Table 7). A further striking difference compared to the a priori inventory is a change in the spatial distribution of emissions over India, which is much more concentrated over the Ganges valley for all inversions which use the SCIAMACHY observations, while the a priori emissions and the emissions derived for sensitivity inversion S3 (using the NOAA data only) exhibit a more homogeneous distribution over the whole country (see Figure 4).

[69] A further interesting feature visible in Figure 13 is the significantly enhanced XCH_4 observed over the Sichuan Basin (also called Red Basin) in China, a region with intensive rice cultivation, but also coal mining and gas production. The enhancement is noticeable throughout the whole year, and shows during the 2nd quarter of the year even the highest XCH_4 values over the entire Asian zoom region.

[70] Overall, the spatial patterns in XCH_4 observed over Asia are well reproduced in the model assimilations. An exception, however, is the tendency to lower simulated XCH_4 values over the Himalaya and Tibetan Plateau. A potential explanation could be that over these regions at very high altitudes systematic errors related to topography and model deficiencies in the stratospheric CH_4 mixing ratios have a larger impact.

5. Conclusions

[71] We have analyzed the impact of the recent revision of the SCIAMACHY retrievals [*Frankenberg et al.*, 2008a] on global and regional CH_4 emission estimates using the TM5-4DVAR inverse modeling system. The significant reduction of column-averaged mixing ratios, XCH_4, over the tropics in the new retrievals (IMAP V5.0) results in a reduction of derived tropical emissions by ~20% (reference inversion S1) compared to an inversion using the previous IMAP V1.1 data set (sensitivity inversion S2). The derived tropical emissions are now very close to an inversion that uses only the NOAA surface measurements (sensitivity inversion S3). However, the SCIAMACHY data put strong constraints on the smaller-scale spatial distribution of emissions, while the remote surface measurements mainly constrain the emissions of larger regions.

[72] The new IMAP V5.0 retrievals provide a much more consistent picture of the global CH_4 distribution compared to IMAP V1.1, which is clearly evident in various aspects: (1) Using the IMAP V5.0 retrievals much better agreement between simulated and observed XCH_4 is achieved, while especially the pronounced tropical XCH_4 enhancement of the IMAP V1.1 retrievals could not be fully reproduced in the model simulations. (2) The new IMAP V5.0 retrievals can be better reconciled with the NOAA surface measurement used simultaneously in the inversion, and lead to better agreement with independent validation data, in particular for the NOAA ocean transects in the tropics and the aircraft measurements in the free troposphere over the Amazon basin [*Miller et al.*, 2007]. (3) The bias correction determined by the TM5-4DVAR system to reconcile satellite and surface measurements is significantly reduced for IMAP V5.0 (by a factor of ~3 compared to IMAP V1.1).

[73] Comparison of NOAA samples from the ocean transects with simulated CH_4 mixing ratios showed very good agreement confirming that the remote surface atmosphere over the ocean is well represented by the model. Also the yearly average vertical gradients within the troposphere measured by the NOAA aircraft profiles are well reproduced at most locations, suggesting that vertical transport is realistically described in TM5. However, more detailed studies should be performed, since vertical transport is very critical for derived emissions [*Stephens et al.*, 2007].

[74] We emphasize that our validation of tropospheric 3D mixing ratio fields mainly demonstrates consistency with different observational data sets and that major patterns of atmospheric variability are realistically simulated, but this does not represent a validation of derived emissions. It is only in the vicinity of significant emissions that the validation of mixing ratios allows some conclusions to be made on the emissions (e.g., for the aircraft profiles over the Amazon).

[75] Validation of simulated stratospheric CH_4 mixing ratios with balloon-borne high-accuracy measurements showed excellent agreement in the tropics and only small deviations at midlatitudes (max $\Delta XCH_{4\ \mathrm{eff}}$ = 7.8 ppb). These small deviations are in the order of the latitudinal component of the derived small bias correction. Hence, it seems conceivable that the remaining bias correction is largely due to deficiencies of the model stratosphere rather than a bias of the retrievals. However, due to the limited number of stratospheric profiles and potential interannual variations and trends, an exact quantification of the potential model bias cannot yet be performed. Balloon-borne measurements at high northern latitudes showed larger discrepancies with model simulations than at midlatitudes or in the tropics because of the influence of the polar vortex. While no SCIAMACHY measurements are made during polar winter, the balloon-borne measurements showed a distinct vortex filament also in June at 68°N. In order to minimize the impact of such structures on the analysis, we generally used only the SCIAMACHY observations between 50°S and 50°N.

[76] A sensitivity experiment replacing the 2nd order polynomial latitudinal bias correction with a (monthly) constant bias correction (sensitivity inversion S5) showed only relatively small differences, demonstrating that with the significant reduction of the bias in the retrievals the correction of the remaining bias is less critical for the analysis.

[77] A further sensitivity experiment showed the importance of assumptions on OH, (the global total of which is currently assumed to be known within ~±10%) affecting mainly the estimates of the large-scale emissions (total emissions of tropics and extratropical SH), while having only a small impact on the derived smaller-scale emission patterns (sensitivity inversion S6). Clearly, further improvements in the estimates of these large-scale emissions critically depend on our knowledge of OH concentration, which becomes very important for the analysis of interannual variations and trends in the atmospheric CH_4 cycle.

[78] Although the smaller-scale spatial emission patterns are significantly constrained by the SCIAMACHY data, the exact model solution depends on the applied a priori

emission inventories. The free inversion (sensitivity inversion S8) results in somewhat different spatial emission patterns especially over South America and Africa, compared to our reference inversion S1. This hints to potential deficiencies of the applied bottom-up inventories, in particular of wetland emissions, which are the most important source in these areas, but could also point to additional sources which were not considered in the present study, such as emissions from plants or geological sources [*Etiope et al.*, 2008]. However, results from the free inversion are much more sensitive to potential systematic observation and model errors and have, therefore, to be viewed with some caution. On the other hand, the free inversion (sensitivity inversion S8) showed a remarkable consistency in derived spatial patterns with our reference inversion in particular for India, China, and Southeast Asia, where the inverse modeling analysis is favored due to the very large signal (and the pronounced seasonality), which is clearly detected by SCIAMACHY. At the same time, the major anthropogenic emissions relevant in Asia (rice cultivation, ruminants and waste) appear to be better quantified in the bottom-up inventories apart from some shortcomings in the spatial distribution within the countries and exact timing of rice emission. In general, this study demonstrates the dependence of derived emissions on the applied a priori inventories, and hence the need for well-validated bottom-up emission inventories with high spatial resolution and monthly or better temporal resolution.

[79] Based on $1^\circ \times 1^\circ$ zoom simulations we presented regional emission estimates for South America, Africa, and Asia. For South America, the high-resolution inversion using the IMAP V5.0 retrievals (inversion S1Z) results in somewhat higher estimates for the wetland emissions from the Amazon basin, the Llanos de Mojos and the Orinoco River plain than the estimates of *Melack et al.* [2004], but values are very close to their estimate for the Pantanal region. Especially the higher values derived for the Llanos de Mojos and the Orinoco River plain are a clear effect of the SCIAMACHY data; however the estimates also depend on the applied a priori inventories. Evidently, further validation of the derived emissions is required. Independent emission estimates on the scales ranging from the size of the model grid cells to larger regions, however, are very difficult to make and require intensive regional measurements. Our study demonstrates that SCIAMACHY measurements provide significant constraints for regional emission estimates especially in the tropics which so far were poorly monitored by the surface network.

[80] **Acknowledgments.** This work has been supported by the European Commission RTD project GEMS (“Global and regional Earth-system (Atmosphere) Monitoring using Satellite and in-situ data,” contract SIP4-CT-2004-516099, 6th Framework Programme). We are grateful to A. Segers for his support concerning the TM5 model framework and assistance in preprocessing the ECMWF meteorological data as TM5 input. We thank John van Aardenne for discussion of emission inventories.

References

Bergamaschi, P. (Ed.) (2007), Atmospheric monitoring and inverse modelling for verification of national and EU bottom-up GHG inventories, *EUR 22893 EN*, 153 pp., Eur. Comm. Joint Res. Cent., Luxembourg.

Bergamaschi, P., M. Krol, F. Dentener, A. Vermeulen, F. Meinhardt, R. Graul, M. Ramonet, W. Peters, and E. J. Dlugokencky (2005), Inverse modelling of national and European CH_4 emissions using the atmospheric zoom model TM5, *Atmos. Chem. Phys.*, *5*, 2431–2460.

Bergamaschi, P., et al. (2006), Model inter-comparison on transport and chemistry: Report on model inter-comparison performed within European Commission FP5 project EVERGREEN (“Global satellite observation of greenhouse gas emissions”), report, 53 pp., Eur. Comm. Joint Res. Cent., Luxembourg.

Bergamaschi, P., et al. (2007), Satellite chartography of atmospheric methane from SCIAMACHY onboard ENVISAT: 2. Evaluation based on inverse model simulations, *J. Geophys. Res.*, *112*, D02304, doi:10.1029/2006JD007268.

Blake, D., and F. Rowland (1988), Continuing worldwide increase in tropospheric methane, *Science*, *239*, 1129–1131, doi:10.1126/science.239.4844.1129.

Bousquet, P., D. A. Hauglustaine, P. Peylin, C. Carouge, and P. Ciais (2005), Two decades of OH variability as inferred by an inversion of atmospheric transport and chemistry of methyl chloroform, *Atmos. Chem. Phys.*, *5*, 2635–2656.

Bousquet, P., et al. (2006), Contribution of anthropogenic and natural sources to atmospheric methane variability, *Nature*, *443*, 439–443.

Brühl, C., and P. J. Crutzen (1993), The MPIC 2D model, *NASA Ref. Publ.*, *1292*, 103–104.

Chen, Y.-H., and R. G. Prinn (2006), Estimation of atmospheric methane emissions between 1996 and 2001 using a three-dimensional global chemical transport model, *J. Geophys. Res.*, *111*, D10307, doi:10.1029/2005JD006058.

Chevallier, F., M. Fisher, P. Peylin, S. Serrar, P. Bousquet, F.-M. Bréon, A. Chédin, and P. Ciais (2005), Inferring CO_2 sources and sinks from satellite observations: Method and application to TOVS data, *J. Geophys. Res.*, *110*, D24309, doi:10.1029/2005JD006390.

Courtier, P., J.-N. Thépaut, and A. Hollingsworth (1994), A strategy for operational implementation of 4D-Var, using an incremental approach, *Q. J. R. Meteorol. Soc.*, *120*, 1367–1387, doi:10.1002/qj.49712051912.

De Mazière, M., et al. (2008), Validation of ACE-FTS v2.2 methane profiles from the upper troposphere to the lower mesosphere, *Atmos. Chem. Phys.*, *8*, 2421–2435.

Denning, A. S., et al. (1999), Three-dimensional transport and concentration of SF6: A model intercomparison study (TransCom 2), *Tellus, Ser. B*, *51*, 266–297.

Dlugokencky, E. J., L. P. Steele, P. M. Lang, and K. A. Masarie (1994), The growth rate and distribution of atmospheric methane, *J. Geophys. Res.*, *99*, 17,021–17,043, doi:10.1029/94JD01245.

Dlugokencky, E. J., S. Houweling, L. Bruhwiler, K. A. Masarie, P. M. Lang, J. B. Miller, and P. P. Tans (2003), Atmospheric methane levels off: Temporary pause or a new steady-state?, *Geophys. Res. Lett.*, *30*(19), 1992, doi:10.1029/2003GL018126.

Dlugokencky, E. J., R. C. Myers, P. M. Lang, K. A. Masarie, A. M. Crotwell, K. W. Thoning, B. D. Hall, J. W. Elkins, and L. P. Steele (2005), Conversion of NOAA atmospheric dry air CH_4 mole fractions to a gravimetrically prepared standard scale, *J. Geophys. Res.*, *110*, D18306, doi:10.1029/2005JD006035.

Dueck, T. A., et al. (2007), No evidence for substantial aerobic methane emission by terrestrial plants: A ^{13}C-labelling approach, *New Phytol.*, *175*, 29–35, doi:10.1111/j.1469-8137.2007.02103.x.

Engel, A., et al. (2006), Observation of mesospheric air inside the arctic stratospheric polar vortex in early 2003, *Atmos. Chem. Phys.*, *6*, 267–282.

Engel, A., et al. (2009), Age of stratospheric air unchanged within uncertainties over the past 30 years, *Nat. Geosci.*, *2*, 28–31, doi:10.1038/ngeo388.

Etheridge, D. M., L. P. Steele, R. J. Francey, and R. L. Langenfelds (1998), Atmospheric methane between 1000 A.D. and present: Evidence of anthropogenic emissions and climatic variability, *J. Geophys. Res.*, *103*(D13), 15,979–15,993, doi:10.1029/98JD00923.

Etiope, G., K. R. Lassey, R. W. Klusman, and E. Boschi (2008), Reappraisal of the fossil methane budget and related emission from geologic sources, *Geophys. Res. Lett.*, *35*, L09307, doi:10.1029/2008GL033623.

Fisher, M., and P. Courtier (1995), Estimating the covariance matrices of analysis and forecast error in variational data assimilation, *Tech. Memo. 220*, Eur. Cent. for Medium-Range Weather Forecasts, Reading, U. K.

Forster, P., et al. (2007), Changes in atmospheric constituents and in radiative forcing, in *Climate Change 2007: The Physical Science Basis. Contribution of Working Group I to the Fourth Assessment Report of the Intergovernmental Panel on Climate Change*, edited by S. Solomon et al., pp. 349–416, Cambridge Univ. Press, Cambridge, U. K.

Frankenberg, C., J. F. Meirink, M. van Weele, U. Platt, and T. Wagner (2005), Assessing methane emissions from global space-borne observations, *Science*, *308*, 1010–1014, doi:10.1126/science.1106644.

Frankenberg, C., J. F. Meirink, P. Bergamaschi, A. P. H. Goede, M. Heimann, S. Körner, U. Platt, M. van Weele, and T. Wagner (2006), Satellite chartography of atmospheric methane from SCIAMACHY onboard ENVISAT: Analysis of the years 2003 and 2004, *J. Geophys. Res.*, *111*, D07303, doi:10.1029/2005JD006235.

Frankenberg, C., P. Bergamaschi, A. Butz, S. Houweling, J. F. Meirink, J. Notholt, A. K. Petersen, H. Schrijver, T. Warneke, and I. Aben (2008a), Tropical methane emissions: A revised view from SCIAMACHY onboard ENVISAT, *Geophys. Res. Lett.*, *35*, L15811, doi:10.1029/2008GL034300.

Frankenberg, C., T. Warneke, A. Butz, I. Aben, F. Hase, P. Spietz, and L. R. Brown (2008b), Pressure broadening in the $2\nu_3$ band of methane and its implication on atmospheric retrievals, *Atmos. Chem. Phys.*, *8*, 5061–5075.

Grooß, J.-U., R. Müller, P. Konopka, H.-M. Steinhorst, A. Engel, T. Möbius, and C. M. Volk (2008), The impact of transport across the polar vortex edge on Match ozone loss estimates, *Atmos. Chem. Phys.*, *8*, 565–578.

Gurney, K. R., et al. (2002), Towards robust regional estimates of CO_2 sources and sinks using atmospheric transport models, *Nature*, *415*, 626–630, doi:10.1038/415626a.

Hein, R., P. J. Crutzen, and M. Heimann (1997), An inverse modeling approach to investigate the global atmospheric methane cycle, *Global Biogeochem. Cycles*, *11*, 43–76, doi:10.1029/96GB03043.

Hirsch, A. I., A. M. Michalak, L. M. Bruhwiler, W. Peters, E. J. Dlugokencky, and P. P. Tans (2006), Inverse modeling estimates of the global nitrous oxide surface flux from 1998–2001, *Global Biogeochem. Cycles*, *20*, GB1008, doi:10.1029/2004GB002443.

Houweling, S., F. Dentener, and J. Lelieveld (1998), The impact of nonmethane hydrocarbon compounds on tropospheric photochemistry, *J. Geophys. Res.*, *103*(D9), 10,673–10,696, doi:10.1029/97JD03582.

Houweling, S., T. Kaminski, F. Dentener, J. Lelieveld, and M. Heimann (1999), Inverse modeling of methane sources and sinks using the adjoint of a global transport model, *J. Geophys. Res.*, *104*(D21), 26,137–26,160, doi:10.1029/1999JD900428.

Houweling, S., T. Röckmann, I. Aben, F. Keppler, M. Krol, J. F. Meirink, E. J. Dlugokencky, and C. Frankenberg (2008), Atmospheric constraints on global emissions of methane from plants, *Geophys. Res. Lett.*, *33*, L15821, doi:10.1029/2006GL026162.

Huang, J., et al. (2008), Estimation of regional emissions of nitrous oxide from 1997 to 2005 using multinetwork measurements, a chemical transport model, and an inverse method, *J. Geophys. Res.*, *113*, D17313, doi:10.1029/2007JD009381.

Intergovernmental Panel on Climate Change (IPCC) (2000), Good practice guidance and uncertainty management in national greenhouse gas inventories, report, Inst. for Global Environ. Strat., Hayama, Japan.

Intergovernmental Panel on Climate Change (IPCC) (2007), *Climate Change 2007: The Physical Science Basis. Contribution of Working Group I to the Fourth Assessment Report of the Intergovernmental Panel on Climate Change*, 996 pp., Cambridge Univ. Press, Cambridge, U. K.

Keppler, F., J. T. G. Hamilton, M. Braß, and T. Röckmann (2006), Methane emissions from terrestrial plants under aerobic conditions, *Nature*, *439*, 187–191, doi:10.1038/nature04420.

Krol, M., and J. Lelieveld (2003), Can the variability in tropospheric OH be deduced from measurements of 1,1,1-trichoreoethane (methyl chloroform)?, *J. Geophys. Res.*, *108*(D3), 4125, doi:10.1029/2002JD002423.

Krol, M. C., S. Houweling, B. Bregman, M. van den Broek, A. Segers, P. van Velthoven, W. Peters, F. Dentener, and P. Bergamaschi (2005), The two-way nested global chemistry-transport zoom model TM5: Algorithm and applications, *Atmos. Chem. Phys.*, *5*, 417–432.

Krol, M. C., J. F. Meirink, P. Bergamaschi, J. E. Mak, D. Lowe, P. Jöckel, S. Houweling, and T. Röckmann (2008), What can ^{14}CO measurements tell us about OH?, *Atmos. Chem. Phys.*, *8*, 5033–5044.

Lambert, G., and S. Schmidt (1993), Reevaluation of the oceanic flux of methane: Uncertainties and long term variations, *Chemosphere Global Change Sci.*, *26*(1–4), 579–589.

Loulergue, L., A. Schilt, R. Spahni, V. Masson-Delmotte, T. Blunier, B. Lemieux, J.-M. Barnola, D. Raynaud, T. F. Stocker, and J. Chappellaz (2008), Orbital and millennial-scale features of atmospheric CH_4 over the past 800,000 years, *Nature*, *453*, 383–386, doi:10.1038/nature06950.

Manning, A. J., D. B. Ryall, R. G. Derwent, P. G. Simmonds, and S. O'Doherty (2003), Estimating European emissions of ozone-depleting and greenhouse gases using observations and a modeling back-attribution technique, *J. Geophys. Res.*, *108*(D14), 4405, doi:10.1029/2002JD002312.

Matthews, E., I. Fung, and J. Lerner (1991), Methane emission from rice cultivation: Geographic and seasonal distribution of cultivated areas and emissions, *Global Biogeochem. Cycles*, *5*, 3–24, doi:10.1029/90GB02311.

Meirink, J. F., et al. (2008a), Four-dimensional variational data assimilation for inverse modelling of atmospheric methane emissions: Analysis of SCIAMACHY observations, *J. Geophys. Res.*, *113*, D17301, doi:10.1029/2007JD009740.

Meirink, J. F., P. Bergamaschi, and M. Krol (2008b), Four-dimensional variational data assimilation for inverse modelling of atmospheric methane emissions: Method and comparison with synthesis inversion, *Atmos. Chem. Phys.*, *8*, 6341–6353.

Melack, J. M., L. L. Hess, M. Gastil, B. R. Forsberg, S. K. Hamilton, I. B. T. Lima, and E. M. L. M. Novo (2004), Regionalization of methane emissions in the Amazon Basin with microwave remote sensing, *Global Change Biol.*, *10*, 530–544, doi:10.1111/j.1365-2486.2004.00763.x.

Mikaloff Fletcher, S. E., P. P. Tans, L. M. Bruhwiler, J. B. Miller, and M. Heimann (2004a), CH_4 sources estimated from atmospheric observations of CH_4 and its $^{13}C/^{12}C$ isotopic ratios: 2. Inverse modelling of CH_4 fluxes from geographical regions, *Global Biogeochem. Cycles*, *18*, GB4005, doi:10.1029/2004GB002224.

Mikaloff Fletcher, S. E., P. P. Tans, L. M. Bruhwiler, J. B. Miller, and M. Heimann (2004b), CH_4 sources estimated from atmospheric observations of CH_4 and its $^{13}C/^{14}C$ isotopic ratios: 1. Inverse modelling of source processes, *Global Biogeochem. Cycles*, *18*, GB4004, doi:10.1029/2004GB002223.

Miller, J. B., L. V. Gatti, M. T. S. d'Amelio, A. M. Crotwell, E. J. Dlugokencky, P. Bakwin, P. Artaxo, and P. P. Tans (2007), Airborne measurements indicate large methane emissions from the eastern Amazon basin, *Geophys. Res. Lett.*, *34*, L10809, doi:10.1029/2006GL029213.

Müller, J.-F., and T. Stavrakou (2005), Inversion of CO and NO_x emissions using the adjoint of the IMAGES model, *Atmos. Chem. Phys.*, *5*, 1157–1186.

Nisbet, R. E. R., et al. (2009), Emission of methane from plants, *Proc. R. Soc., Ser. B*, *276*, 1347–1354, doi:10.1098/rspb.2008.1731.

Olivier, J. G. J., and J. J. M. Berdowski (2001), Global emissions sources and sinks, in *The Climate System*, edited by J. J. M. Berdowski et al., pp. 33–78, A. A. Balkema, Lisse, Netherlands.

Peters, W., M. C. Krol, L. Bruhwiler, E. J. Dlugokencky, G. Dutton, J. B. Miller, P. Bergamaschi, F. J. Dentener, P. van Velthoven, and P. P. Tans (2004), Toward regional scale inversion using a two-way nested global model: Characterization of transport using SF_6, *J. Geophys. Res.*, *109*, D19314, doi:10.1029/2004JD005020.

Peters, W., J. B. Miller, J. Whitaker, A. S. Denning, A. Hirsch, M. C. Krol, D. Zupanski, L. Bruhwiler, and P. P. Tans (2005), An ensemble data assimilation system to estimate CO_2 surface fluxes from atmospheric trace gas observations, *J. Geophys. Res.*, *110*, D24304, doi:10.1029/2005JD006157.

Peters, W., et al. (2007), An atmospheric perspective on North American carbon dioxide exchange: CarbonTracker, *Proc. Natl. Acad. Sci. U. S. A.*, *104*(48), 18,925–18,930, doi:10.1073/pnas.0708986104.

Prinn, R. G., D. Cunnold, R. Rasmussen, P. Simmonds, F. Alyea, A. Crawford, P. Fraser, and R. Rosen (1990), Atmospheric emissions and trends of nitrous oxide deduced from ten years of ALE/GAGE data, *J. Geophys. Res.*, *95*, 18,369–18,385, doi:10.1029/JD095iD11p18369.

Randel, W. J., F. Wu, J. M. Russell III, A. Roche, and J. W. Waters (1998), Seasonal cycles and QBO variations in stratospheric CH_4 and H_2O observed in UARS HALOE data, *J. Atmos. Sci.*, *55*, 163–185, doi:10.1175/1520-0469(1998)055<0163:SCAQVI>2.0.CO;2.

Ridgwell, A. J., S. J. Marshall, and K. Gregson (1999), Consumption of atmospheric methane by soils: A process-based model, *Global Biogeochem. Cycles*, *13*(1), 59–70, doi:10.1029/1998GB900004.

Rigby, M., et al. (2008), Renewed growth of atmospheric methane, *Geophys. Res. Lett.*, *35*, L22805, doi:10.1029/2008GL036037.

Rödenbeck, C., S. Houweling, M. Gloor, and M. Heimann (2003), CO_2 flux history 1982–2001 inferred from atmospheric data using a global inversion of atmospheric transport, *Atmos. Chem. Phys.*, *3*, 1919–1964.

Rohs, S., C. Schiller, M. Riese, A. Engel, U. Schmidt, T. Wetter, I. Levin, T. Nakazawa, and S. Aoki (2006), Long-term changes of methane and hydrogen in the stratosphere in the period 1978–2003 and their impact on the abundance of stratospheric water vapor, *J. Geophys. Res.*, *111*, D14315, doi:10.1029/2005JD006877.

Sanderson, M. G. (1996), Biomass of termites and their emissions of methane and carbon dioxide: A global database, *Global Biogeochem. Cycles*, *10*, 543–557, doi:10.1029/96GB01893.

Schneising, O., M. Buchwitz, J. P. Burrows, H. Bovensmann, P. Bergamaschi, and W. Peters (2009), Three years of greenhouse gas column-averaged dry air mole fractions retrieved from satellite—Part 2: Methane, *Atmos. Chem. Phys.*, *9*, 443–465.

Shindell, D. T., G. Faluvegi, N. Bell, and G. Schmidt (2005), An emissions-based view of climate forcing by methane and tropospheric ozone, *Geophys. Res. Lett.*, *32*, L04803, doi:10.1029/2004GL021900.

Spahni, R., et al. (2005), Atmospheric methane and nitrous oxide of the late Pleistocene from Antarctic ice cores, *Science*, *310*, 1317–1321, doi:10.1126/science.1120132.

Spivakovsky, C. M., et al. (2000), Three-dimensional climatological distribution of tropospheric OH: Update and evaluation, *J. Geophys. Res.*, *105*(D7), 8931–8980, doi:10.1029/1999JD901006.

Stavrakou, T., and J.-F. Müller (2006), Grid-based versus big region approach for inverting CO emissions using Measurement of Pollution in the

Troposphere (MOPITT) data, *J. Geophys. Res.*, *111*, D15304, doi:10.1029/2005JD006896.

Stemmler, K., D. Folini, S. Ulb, M. K. Vollmer, S. Reimann, S. O'Doherty, B. R. Greally, P. G. Simmonds, and A. J. Manning (2007), European emissions of HFC-365mfc, a chlorine-free substitute for the foam blowing agents HCFC-141b and CFC-11, *Environ. Sci. Technol.*, *41*, 1145–1151, doi:10.1021/es061298h.

Stephens, B. B., et al. (2007), Weak northern and strong tropical land carbon uptake from vertical profiles of atmospheric CO_2, *Science*, *316*, 1732–1735, doi:10.1126/science.1137004.

Tremolet, Y. (2007), Incremental 4D-Var convergence study, *Tellus, Ser. A*, *59*, 706–718.

van der Werf, G. R., J. T. Randerson, G. J. Collatz, L. Giglio, P. S. Kasibhatla, A. F. Arellano Jr., S. C. Olsen, and E. S. Kasischke (2004), Continental-scale partitioning of fire emissions during the 1997 to 2001 El Niño/La Niña period, *Science*, *303*, 73–76, doi:10.1126/science.1090753.

Vigano, I., H. van Weelden, R. Holzinger, F. Keppler, A. McLeod, and T. Röckmann (2008), Effect of UV radiation and temperature on the emission of methane from plant biomass and structural components, *Biogeosciences*, *5*, 937–947.

P. Bergamaschi, F. Dentener, and M. G. Villani, Institute for Environment and Sustainability, European Commission Joint Research Centre, I-21027 Ispra VA, Italy. (peter.bergamaschi@jrc.it)

E. J. Dlugokencky and J. B. Miller, Global Monitoring Division, Earth System Research Laboratory, NOAA, Boulder, CO 80305, USA.

A. Engel, Institute for Atmosphere and Environment, J.W. Goethe University, D-60054 Frankfurt am Main, Germany.

C. Frankenberg, S. Houweling, and M. Krol, Netherlands Institute for Space Research, SRON, NL-3584 CA Utrecht, Netherlands.

L. V. Gatti, Instituto de Pesquisas Energeticas Nucleares, Pinheiros, SP 5542-970, Brazil.

I. Levin, Institute of Environmental Physics, University of Heidelberg, D-69120 Heidelberg, Germany.

J. F. Meirink, Royal Netherlands Meteorological Institute, NL-3732 GK De Bilt, Netherlands.